Doppler Radar Observations of Horizontal Shearing Instability in Quasi-Linear Convective Systems

DUSTIN M. CONRAD AND KEVIN R. KNUPP

University of Alabama in Huntsville, Huntsville, Alabama

ABSTRACT

Dual-Doppler radar observations of two cold-season, wave-propagating quasi-linear convective systems (QLCS), which evolved in high-shear, low-CAPE (HSLC) environments, are analyzed to determine the role that horizontal shearing instability (HSI) plays in the formation of mesovortices. One QLCS occurred on 4 January 2015 and produced two mesovortices within the dual-Doppler region, one of which was associated with an EF-1 tornado with a pathlength of 10 km. The second QLCS occurred on 28 November 2016 and did not produce any mesovortices. Storm characteristics such as the low-level wind speed and wind shift angle are investigated. Rayleigh and Fjørtoft instability criteria, which are required but insufficient for HSI, are also examined. The Rayleigh and Fjørtoft instability criteria are satisfied for the 4 January 2015 QLCS and the 28 November 2016 QLCS, highlighting one of the issues of the ''required, but insufficient'' characteristic of the criteria. Analysis of the wind shift angle and wind speed agree with previous studies that pronounced wind shifts close to 90° and strong wind speeds were conducive to the formation of mesovortices, while weak wind shift angles and weaker wind speeds were not. It was found that for the 4 January 2015 case, HSI was the likely formation mechanism of the vortices as other features associated with preexisting mesovortexgenesis theories were not observed.

1. Introduction

In the continental United States, quasi-linear convective systems (QLCS) occur throughout the entire year and are known for primarily producing damaging winds and/or tornadoes. They tend to occur at night in a wide range of vertical wind shears and buoyancy profiles [convective available potential energy (CAPE); Markowski and Richardson (2010)]. According to previous studies, the southeastern United States experiences an average of 30–40 tornado days annually due to mesoscale convective systems (MCS) (Knupp et al. 1996; Trapp et al. 2005). During the cold season in the southeast (October–March), QLCSs are more likely to occur in a high-shear, low-CAPE (HSLC) environment, which is characterized as surface-based CAPE less than $500 \, \mathrm{J \, kg^{-1}}$ and 0–6-km bulk wind shear greater than $18 \, \mathrm{m \, s^{-1}}$ (Sherburn and Parker 2014). HSLC QLCSs have recently become a focus of researchers and operational meteorologists due to their ability to produce mesovortices (vortex width 4–400-km diameter;

Markowski and Richardson 2010) and tornadoes in environments that have historically been deemed unfavorable for HSLC QLCS tornadoes (Schneider et al. 2006; Schneider and Dean 2008; Guyer and Dean 2010; Davis and Parker 2014; Sherburn and Parker 2014).

Multiple hypotheses exist in the literature explaining different processes that lead to mesovortexgenesis in QLCSs. One theory involves the tilting of horizontal vorticity ahead of the QLCS generated by the storm's baroclinic zone. This tilted horizontal vorticity is then subsequently stretched by the updraft (Atkins and Laurent 2009a,b, hereafter AL09). This theory leads to the ingestion of streamwise vorticity and produces only cyclonic vortices along the leading edge. AL09 also suggest that during the early stages in a QLCS life cycle, a downdraft outflow can accelerate the gust front, causing it to bow out and increase low-level convergence and vertical motion. This tilts the horizontal vorticity generated by the gust front baroclinic zone, leading to the ingestion of crosswise vorticity and the formation of a cyclonic and anticyclonic couplet. Other finescale observations of meso- and misovortices (vortex width 40–4000-m diameter; Markowski and Richardson 2010) show similar characteristics with the upward tilting of horizontal

Corresponding author: Dustin M. Conrad, dconrad@nsstc.uah.edu

TABLE 1. ARMOR and KHTX radar VCP specifications for 4 Jan 2015 and 28 Nov 2016 QLCSs.

	KHTX	ARMOR (4 Jan 2015)	ARMOR (28 Nov 2016)
Band (wavelength, λ) $\lambda = c/f$	S band (10 cm)	C band (5 cm)	C band (5 cm)
Frequency (f, MHz)	2700–3000	5625	5625
Half-power beamwidth (°)	0.925	1.0	1.0
Gate spacing (m)	250	250	125
Max unambiguous range (km)	230	125	125
Elevation angles (°)	0.5–19.5 (14 tilts)	0.7–3.4 (5 tilts)	0.7–16.0 (11 tilts)
Volume scan times (min)	4.5	2.5	5

vorticity, generated by horizontal convective rolls, by the gust front of the QLCS (Atkins et al. 1998).

Other studies have proposed that horizontal vorticity is tilted downward, but with different source regions. Trapp and Weisman (2003, hereafter TW03) and Weisman and Trapp (2003, hereafter WT03) suggest that the source region varies during the life cycle of the QLCS, with the source region being directly behind the gust front in the early stages, and underneath the rear inflow jet (RIJ), located on top of the cold pool, in the mature stages. Both source regions lead to the formation of a cyclonic and anticyclonic couplet. A common theme between other modeling and observational studies is that stretching plays a vital role in intensification of mesovortices as increases in the vertical vorticity are seen with increased convergence and vertical motion (Wakimoto and Wilson 1989; Weisman and Davis 1998; Wheatley and Trapp 2008; Schenkman et al. 2012; Xu et al. 2015b,a).

Given the strong horizontal shear that is typically located parallel to the leading edge of cold-season, HSLC QLCSs, the release of horizontal shearing instability (HSI) has been hypothesized as an additional potential mechanism of mesovortexgenesis. Shear instability within the vertical plane (Kelvin–Helmholtz) and horizontal plane (HSI) extracts energy from the mean flow, converting it into discrete maxima of vorticity (Haurwitz 1949; Markowski and Richardson 2010). HSI has been hypothesized to be responsible for the formation of small-scale vortices within vigorous narrow cold frontal rainbands (NCFR; Carbone 1982, 1983; Kawashima 2011), outflow boundaries (Mueller and Carbone 1987; Wakimoto and Wilson 1989; Lee and Wilhelmson 1997a,b, hereafter LW97), and idealized near-surface boundaries (Buban and Ziegler 2016a,b, hereafter BZ16). LW97 found that lobe and cleft instabilities, which develop near the outflow nose, can trigger HSI and the formation of misovortices which undergo a life cycle of vortex sheet roll up, subharmonic interaction, consolidation, and dissipation. Buban et al. (2012) also show that in a numerical simulation of a dryline, the roll up of a vertical vortex sheet agrees with previous studies of vortex formation within sheared flow.

Because of the short life cycle of meso- and misovortices along boundaries, only a few observational studies of vortices inferred to have been generated by HSI have been conducted. During the International H_2O Project (IHOP), surface boundaries, such as cold fronts and drylines, were observed at high resolution with mobile Doppler radars. Mesovortices along these boundaries displayed increased vertical motion and created favored regions for lifting and cloud formation (Arnott et al. 2006). Marquis et al. (2007) noted that these vortices likely formed as a result of HSI, even though no vortex sheet roll-up was observed. Przybylinski (1995) observed circulations forming in regions of relatively greater horizontal shear along the leading edge of a bow echo that occurred on 2 July 1992. Other observational studies have noted similar features with vortices forming in regions of greater horizontal wind shear at the leading edge of bow echoes and QLCSs
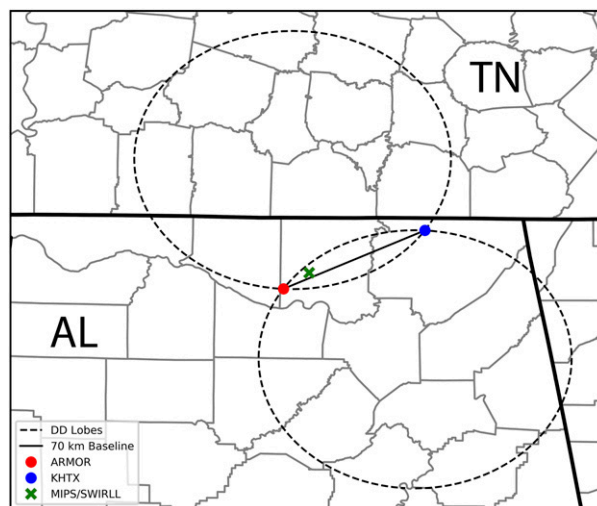

FIG. 1. Domain for both QLCS events in north Alabama. Dual-Doppler lobes [dashed lines are $\beta = 30°$; where β is the angle subtended by the radar beams (Doviak and Zrnic 1993)] are given by dashed rings with the baseline given by the solid black line. Radar locations are given by circles (red: ARMOR, blue: KHTX). Location of the MIPS and RaDAPS profilers (located at the UAH SWIRLL facility) is the green ×.

TABLE 2. MIPS sensors and their measurement characteristics.

Instrument	Quantities measured or calculated	Measurement height	Vertical resolution	Temporal resolution	Dwell time
Vertically pointing X-band radar (XPR)	Reflectivity, mean velocity, spectral width	Surface–20 km	50 m	Pulse duration: 0.99, 0.38, or 0.19 μs	0.17 s
915-MHz Doppler Wind Profiler	Signal-to-noise ratio, vertical velocity, spectral width, horizontal wind, Doppler spectra	0.17–4 km (default), 0.17–10 km in precipitation in some cases	57 m	60 s (vertical beam), 10–30 min (wind profiles)	30 s
Microwave Profiling Radiometer (MPR)	Temperature and water vapor profiles	Surface–10 km	Variable, scales with height 100 m from surface to 1 km, then 250 m up to 10 km	1 min	—
Ceilometer	Attenuated backscatter, cloud base	10 m–15 km	10 m	15–120 s	15–120 s

(e.g., Forbes and Wakimoto 1983; Knupp et al. 1996), which may be caused by the release of HSI.

The objective of this study is to investigate the hypothesis that the release of HSI produced mesovortices within one of two QLCSs observed over northern Alabama. One QLCS produced mesovortices that formed in a manner consistent with HSI (4 January 2015), while the other did not produce mesovortices (28 November 2016). The 28 November 2016 QLCS was selected over other null cases as it occurred a HSLC environment, did not have storm-scale features required by the other hypotheses of mesovortexgenesis, and occurred within dual-Doppler coverage during an intensive operating period of the VORTEX-SE field campaign. Section 2 outlines data and methods used for this study. Section 3 provides an analysis of the kinematics of the two QLCSs using a dual-Doppler analysis, where the Rayleigh and Fjørtoft criteria are hypothesized to be met for 4 January 2015, but not 28 November 2016. Summary and conclusions are presented in section 4.

2. Data and methodology

The University of Alabama in Huntsville (UAH) Advanced Radar for Operational and Meteorological Research (ARMOR), the UAH Mobile Integrated Profiling System (MIPS), the UAH Rapidly Deployable Atmospheric Profiling System (RaDAPS; 28 November 2016 event only), and the WSR-88D in Hytop, Alabama (KHTX), collected data during QLCS passages in northern Alabama on 4 January 2015 and 28 November 2016. Radar and volume coverage pattern (VCP) specifications are given in Table 1. ARMOR is located

TABLE 3. RaDAPS sensors and their measurement characteristics.

Instrument	Quantities measured or calculated	Measurement height	Vertical resolution	Temporal resolution	Dwell time
Micro-Rain Radar (MRR)	Reflectivity, fall velocity, liquid water content, drop spectra, rainfall rate, spectral reflectivity, attenuation	Surface–3 km	30–100 m	User selectable 10–3600 s	User selectable 10–3600 s
915 MHz Doppler Wind Profiler	Signal-to-Noise ratio, vertical velocity, spectral width, horizontal wind, Doppler spectra	0.17–3 km (clear air), 0.17–5 km in precipitation in some cases	75–500 m	5-min consensus	35 s
Microwave Profiling Radiometer (MPR)	Temperature and water vapor profiles	Surface–10 km	Variable, scales with height 100 m from surface to 1 km, then 250 m up to 10 km	1 min	—
Ceilometer	Attenuated backscatter, cloud base	10 m–15 km	10 m	15–120 s	15–120 s

TABLE 4. Grid dimensions and characteristics for both QLCS events. The dual- Doppler effective resolution was determined using Davies-Jones (1979).

	4 Jan 2015	28 Nov 2016
Grid size ($X \times Y \times Z$)	180 km $\times$ 120 km $\times$ 7.5 km	90 km $\times$ 105 km $\times$ 10 km
Horizontal grid spacing	1000 m	1000 m
Dual-Doppler effective resolution	1.4 km	1.5 km
Vertical grid spacing	500 m	500 m
Grid rotation	0°	18°

at the Huntsville International Airport on the west side of Huntsville, Alabama, resulting in dual-Doppler lobes oriented in a northwest–southeast fashion with a 70-km baseline. The locations of all radars, MIPS/RaDAPS, and approximate dual-Doppler lobes are given in Fig. 1. Tables 2 and 3 list the sensors and their measurement characteristics for the MIPS and RaDAPS platforms.

Data from KHTX and ARMOR were edited using the National Center for Atmospheric Research's (NCAR) Solo3 software (Oye et al. 1995; Bell et al. 2013). Areas of ground clutter (radial velocity +2 and −2 m s⁻¹, cross-correlation coefficient below 0.8 and 0.7, reflectivity above 50 dBZ), second trip echo (reflectivity below 20 dBZ and highly speckled radial velocity), and noise (small groupings of pixels with low reflectivity and cross-correlation coefficient) were manually determined from horizontal reflectivity Z_H, radial velocity V_R, differential reflectivity Z_{DR}, and cross-correlation coefficient ρ_{HV} and were removed. Manual unfolding of V_R was performed on both ARMOR (16.1 m s⁻¹ Nyquist velocity) and KHTX (Nyquist velocity between 21 and 35 m s⁻¹) data. Data were interpolated to a common Cartesian grid of different sizes (Table 4) using the NCAR Radx software (Dixon and Wiener 1993). For the 28 November 2016 QLCS, the grid was rotated so that the leading edge of the QLCS was orientated parallel to the y axis. Since the 4 January 2015 QLCS was oriented along the north–south direction, no rotation was required.

Three-dimensional wind syntheses were performed using the NCAR CEDRIC software (Mohr et al. 1986). The grid origin for the dual-Doppler analyses is the location of KHTX for both events. To reduce temporal errors with the 4 January 2015 QLCS, only ARMOR volume scans that were fully within a KHTX volume scan (temporally) were used for the wind synthesis. For the 28 November 2016 QLCS, temporal issues are of minor concern as volume scans for both radars began and ended within one minute of each other. A downward integration of the anelastic mass continuity equation was used in Eq. (1):
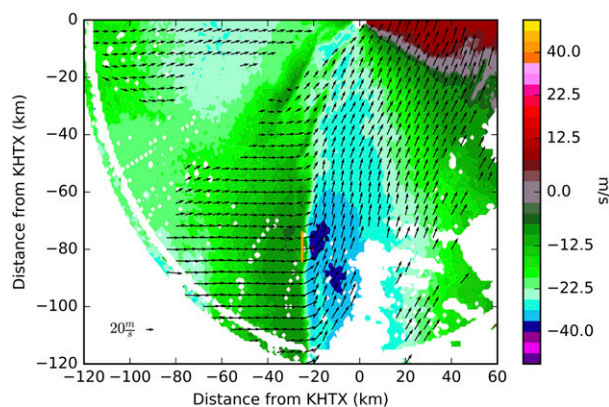

FIG. 2. Example of how the averaged winds were calculated. ARMOR is located near ($x = -60$, $y = -32$). Location of the surface data and UAH is near ($x = -58$, $y = -32$). Vectors at 1.5 km MSL (about 1.2 km AGL) represent the horizontal winds from the dual-Doppler synthesis. Scale is provided in the figure. A 10-km swath represented by the orange line centered on the mesovortex (in this example, the northern mesovortex), where the winds are averaged on the orange line for every x value. Colors define radial velocity from KHTX. Image is from the 4 Jan 2015 QLCS.

$$\nabla \cdot (\rho \mathbf{U}) = 0. \qquad (1)$$

From these wind syntheses, vertical vorticity and horizontal winds were calculated and analyzed. Given the inherent uncertainties with the downward integration in the 4 January 2015 event, vertical velocity and fields calculated using vertical velocity are not used. This is due to ARMOR not scanning above the top of the convection (the highest altitude ARMOR data level was only 3 km, 4 km lower that from KHTX; ARMOR Z_H maximum value near 55 dBZ) and incomplete sampling below 1.2 km mean sea level (MSL) [about 1 km above ground level (AGL)] due to the 70-km distance of the features of interest.

Sources of error in the dual-Doppler retrieval include the elevation differences between the two radars leading to sampling of different heights of the storm for similar elevation angles in a vertically sheared environment, timing differences between the lowest elevation angle scan of the two radars, and sampling within regions of strong horizontal shear at a distance of near 70 km (location of tornadic vortex) from the radar. Since both ARMOR and KHTX were able to capture the vertical extent of the storm for the 28 November 2016 QLCS and the volume scans began within one minute of each other, temporal errors should be minimized. For the 4 January 2015 QLCS, errors within the dual-Doppler retrieval are more significant given the timing differences between the beginning of each respective radar volume and the inability to capture the vertical extent of the storm. The error associated with these is on the order of
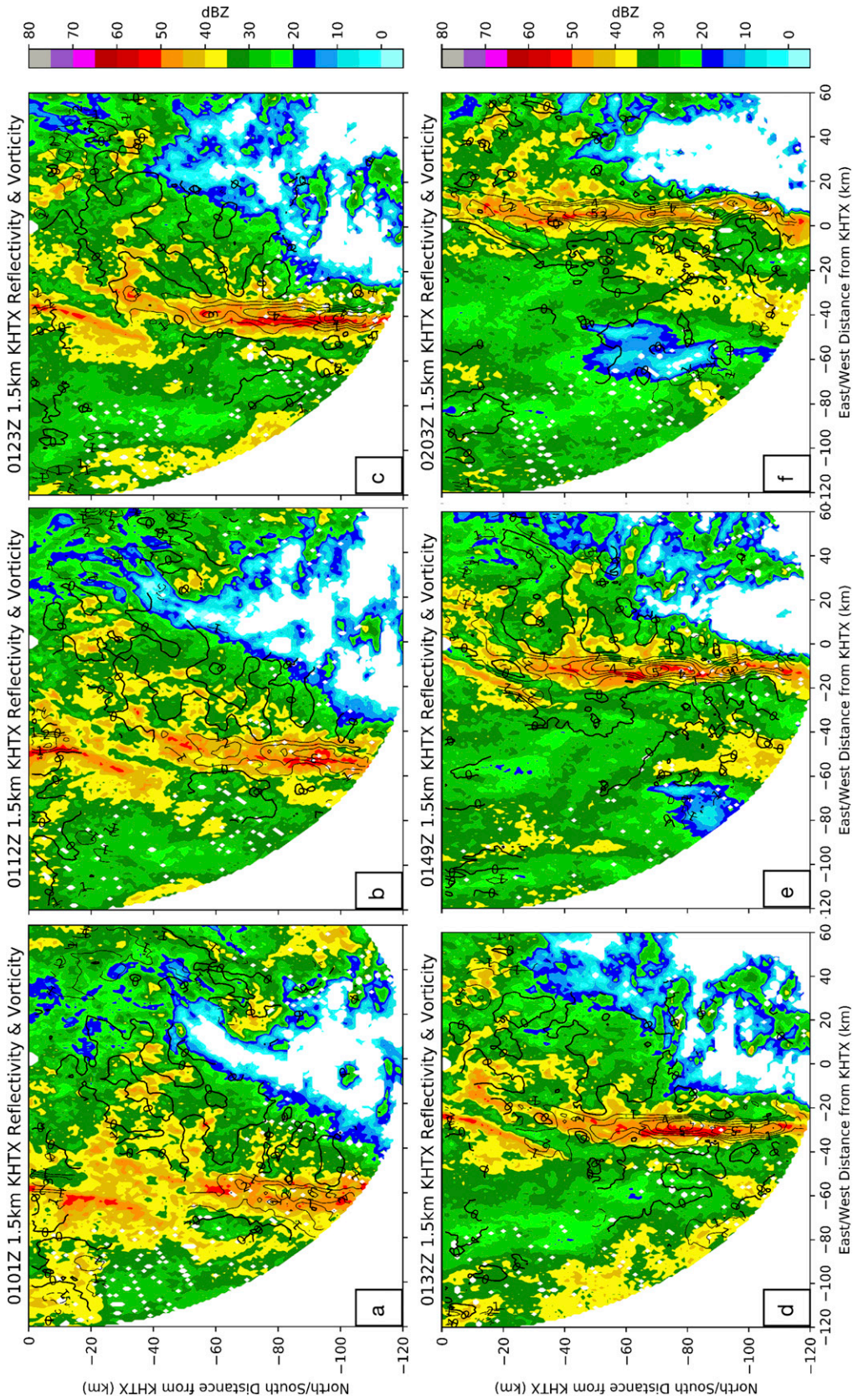
FIG. 3. Overview of 4 Jan 2015 QLCS at (a) 0101, (b) 0112, (c) 0123, (d) 0132, (e) 0149, and (f) 0203 UTC; reflectivity from KHTX with vertical vorticity (1×10^{-3} s^{-1} contours). Negative values of vorticity have dashed contours. Bold shows the 0×10^{-3} s^{-1} contour. Location of the surface data and UAH is near ($x = -58$, $y = -32$).
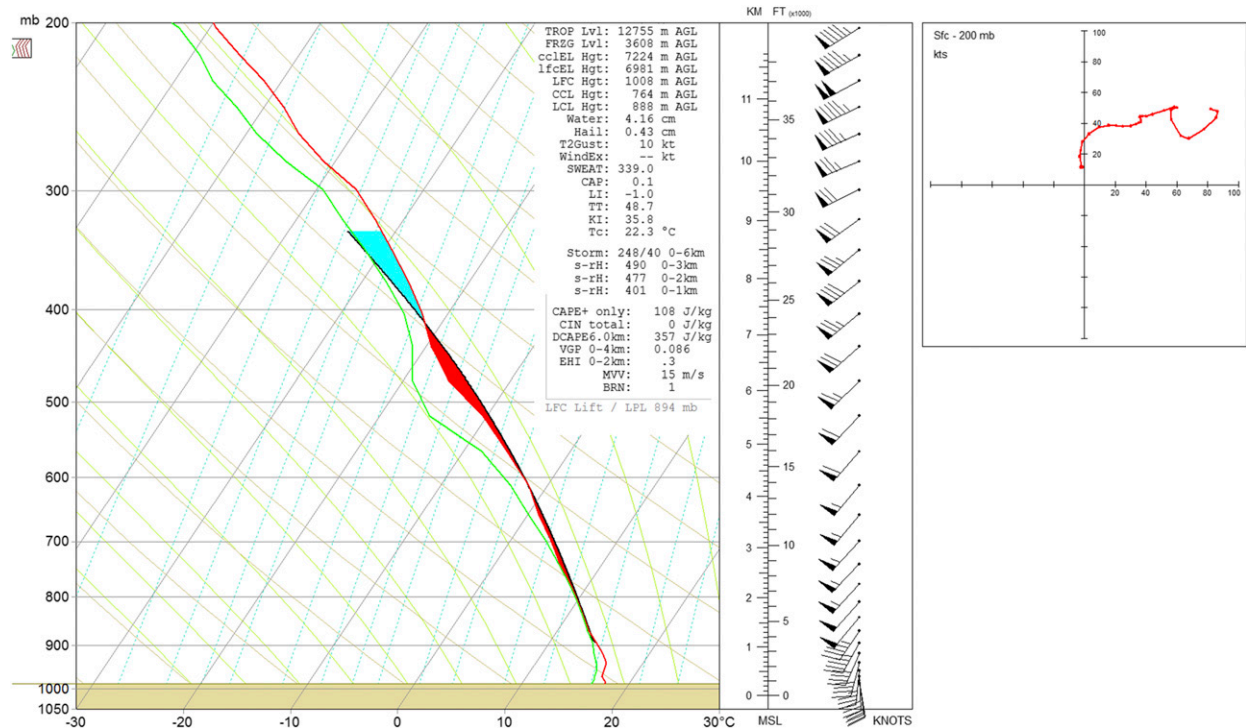
FIG. 4. RAP model sounding at 0100 UTC 4 Jan 2015 near the location of the tornadic mesovortex. Red (green) line is temperature (dewpoint) in °C. Black line indicates parcel temperature, while red shading is positive buoyant energy and blue is negative buoyant energy.

4–6 m s^{-1} for vertical motion w and 1–3 m s^{-1} for the horizontal wind (Doviak et al. 1976; Chong et al. 1983). Given the 1-km grid spacing and the 1-km radius of influence, the impact of these errors should be reduced to a certain degree.

3. Kinematics

To determine if HSI played a role in the two QLCS events, instability criteria were calculated using the dual-Doppler wind syntheses. The Rayleigh and Fjørtoft instability criteria define two criteria that are required, but insufficient for HSI to occur. The Rayleigh instability criterion valid for mesoscale phenomenon [Eq. (2); Rayleigh 1879; Drazin and Howard 1966; Marchioro and Pulvirenti 1994; Sun 2007; Markowski and Richardson 2010] indicates that an inflection point is located in the flow, as determined by

$$\frac{\partial^2 \overline{v}}{\partial x^2} = 0 \,(\text{inflection point}), \qquad (2)$$

where $\overline{v}$ is the average wind speed parallel to the leading edge of the QLCS and x is the direction normal to the leading edge. The average wind speed ($\overline{v}$) is used to smooth out the effects of the vortex itself. A change in

sign located near the wind shift indicates that an inflection point is present and may be unstable for HSI release. For both events, winds were averaged along a 10-km segment in the y direction parallel to the leading edge of the QLCS at each x. The average $\overline{v}$ is determined for a range of v values in the x direction on each side of the wind shift along a 10-km swath in the y direction, as shown by the orange line in Fig. 2.

The Fjørtoft criterion valid for mesoscale phenomenon, defined by

$$\frac{\partial^2 \overline{v}}{\partial x^2}(\overline{v} - \overline{v}_I) < 0 \qquad (3)$$

is a more stringent condition, where $\overline{v}_I$ is the wind speed parallel to the leading edge at the inflection point. The Fjørtoft criterion is satisfied for shearing instability when the criterion is less than 0 on both sides of the inflection point (Fjørtoft 1950; Drazin and Howard 1966; Marchioro and Pulvirenti 1994; Sun 2007; Markowski and Richardson 2010).

In addition to the Rayleigh and Fjørtoft criteria, the wind speed change and wind shift angle in the zonal direction were determined. Clark and Parker (2014, hereafter CP14) performed an observational analysis of surface wind data within vigorous NCFRs over the
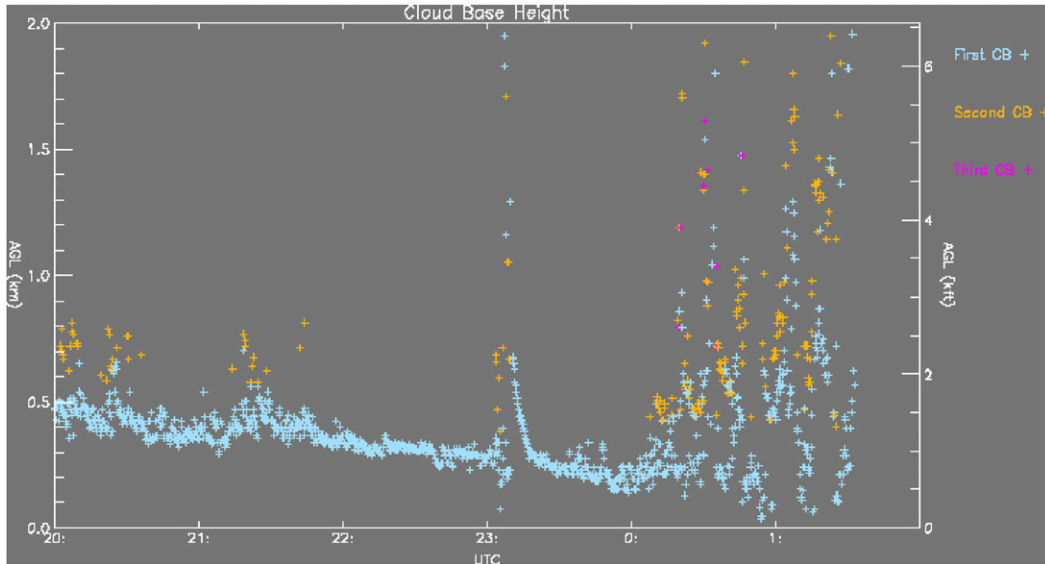
FIG. 5. Ceilometer cloud-base height from the UAH MIPS on 3 Jan 2015. Precipitation arrived at the MIPS location around 2300 UTC. Cloud-base height, which is inferred to be the LCL height, is near 125 m AGL near 0000 UTC. Pluses (+) represent the cloud-base height at the first (blue), second (orange), and third (pink) cloud base. Derived cloud-base height becomes noisy during rain, starting shortly at 0015 UTC.

United Kingdom and found the following three primary thresholds that distinguished between tornadic and nontornadic NCFRs. A wind shift with a large veer (angle close to or greater than 90°) and strong total horizontal wind speeds for both pre and postfrontal winds were associated with tornadic NCFRs, while a small veer (≤45°–50°), but strong pre and postfrontal winds were nontornadic. CP14 also concluded that
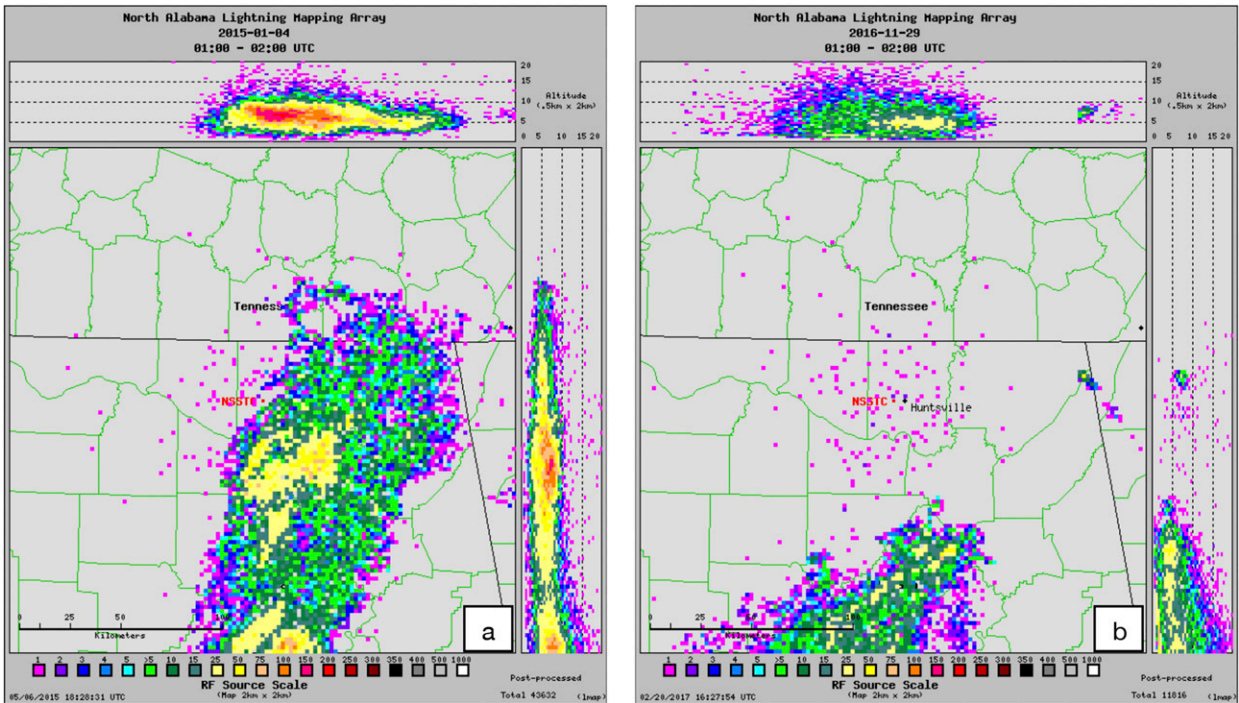

FIG. 6. Lightning source density from the North Alabama Lightning Mapping Array (NALMA) from 0100 to 0200 UTC for (a) 4 Jan 2015 and (b) 28 Nov 2016. Points indicate number of radio frequency (RF) sources in pixel. Top and side inset panels display sources with height in the (top inset) x direction and (side inset) y direction for the entirety of the plan view.
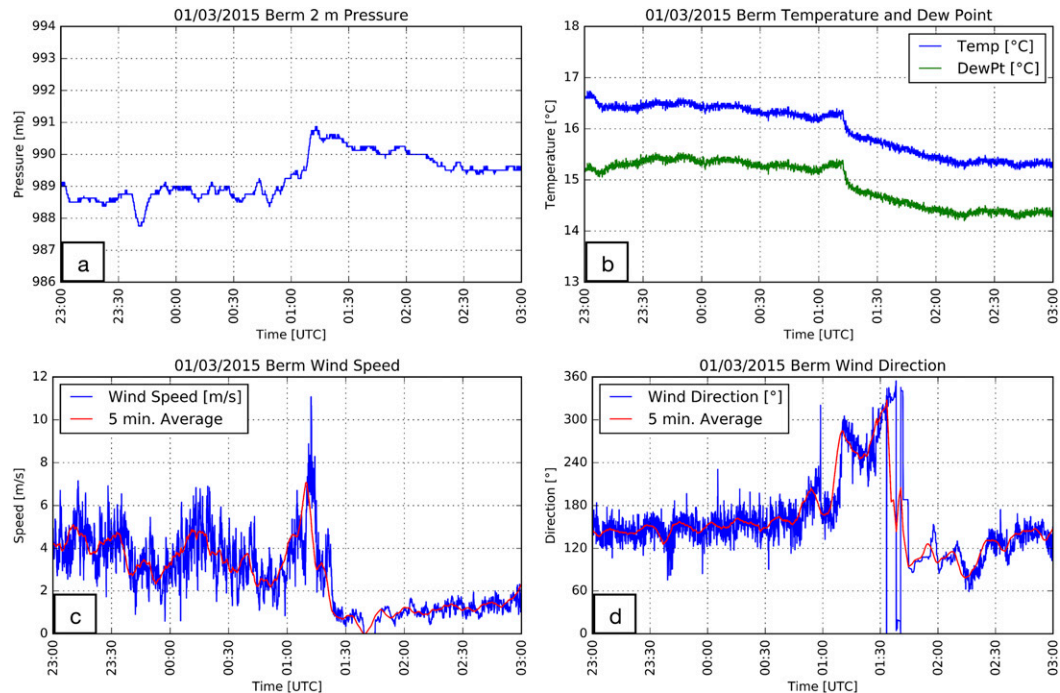
FIG. 7. Time series of (a) 2-m pressure, (b) 2-m temperature/dewpoint, (c) 10-m wind speed, and (d) 10-m wind direction from the UAH SWIRLL facility (berm). QLCS passage over instrumentation occurred shortly after 0100 UTC. The RH sensor has a low bias that is estimated to lead to a 1°C low bias in the derived dewpoint; the air is likely close to saturation during this entire time period.

weak, postfrontal winds were not conducive for torna-dogenesis even if the wind shift angle was large.[1] These criteria will serve as a basis to identify whether or not HSI played a role in mesovortexgenesis for each QLCS in our study.

a. 4 January 2015 (tornadic QLCS)

On 4 January 2015, a QLCS extending from southern Tennessee to central Alabama propagated across the northern Alabama mesoscale domain during the early evening hours. From 2330 to 0030 UTC the QLCS be-came slabular (i.e., an unbroken two-dimensional swath of ascent, James et al. (2005)) over the northern half of Alabama and developed a trailing stratiform region. Within the dual-Doppler domain, the wind shift at the leading edge of the QLCS became more pronounced

and the QLCS maintained a forward propagation speed of near 16 m s^{-1} (Fig. 3).

The QLCS evolved in an HSLC environment as sug-gested by a sounding from the Rapid Refresh (RAP) model which depicted most-unstable CAPE of 108 J kg^{-1} (Fig. 4). The sounding also indicated 28.3 m s^{-1} of surface–6-km bulk shear, which meets the definition of a HSLC environment given in section 1. The lifting condensation level (LCL) height of a surface-based parcel (approximately 200 m MSL) was similar to the cloud base height measured by the UAH MIPS ceilometer (125 m AGL) at 2300 UTC prior to the arrival of the QLCS. Low-level clouds with a cloud base near 300 m AGL were present well before the arrival of the QLCS (Fig. 5).[2] Although updraft in-formation is not available from the dual-Doppler anal-ysis for this case, Fig. 6a shows lightning activity associated with the storm, implying maximum updraft speeds of at least 10 m s^{-1} (Deierling and Petersen 2008). Figure 7 shows surface measurements of pressure, 2-m temperature and dewpoint, and 10-m wind speed and di-rection from the MIPS site. The leading edge of the QLCS

---

[1] The terminology of strong/weak is used throughout the rest of this manuscript to keep consistent with the results of CP14, since they do not provide quantitative wind speed in their thresholds. Although further investigation is needed to determine precise thresholds, loose criteria for this study consider winds (at about 1.2 km AGL) 2 km east and 2 km west of the leading edge of the QLCS above 30 m s^{-1} to be strong while a wind shift angle of 80° is considered large. These are values at about 1.2 km AGL. Further research is needed to better quantify wind speed and direction changes over the layer from the surface to about 1 km AGL.

[2] Since the 915-MHz wind profiler is unable to sample up to 6 km outside of precipitation (highest wind retrieval was near 2 km AGL) for this case and MPR thermodynamic retrievals have low resolution above 3 km AGL, these remote sensing observations are not used.
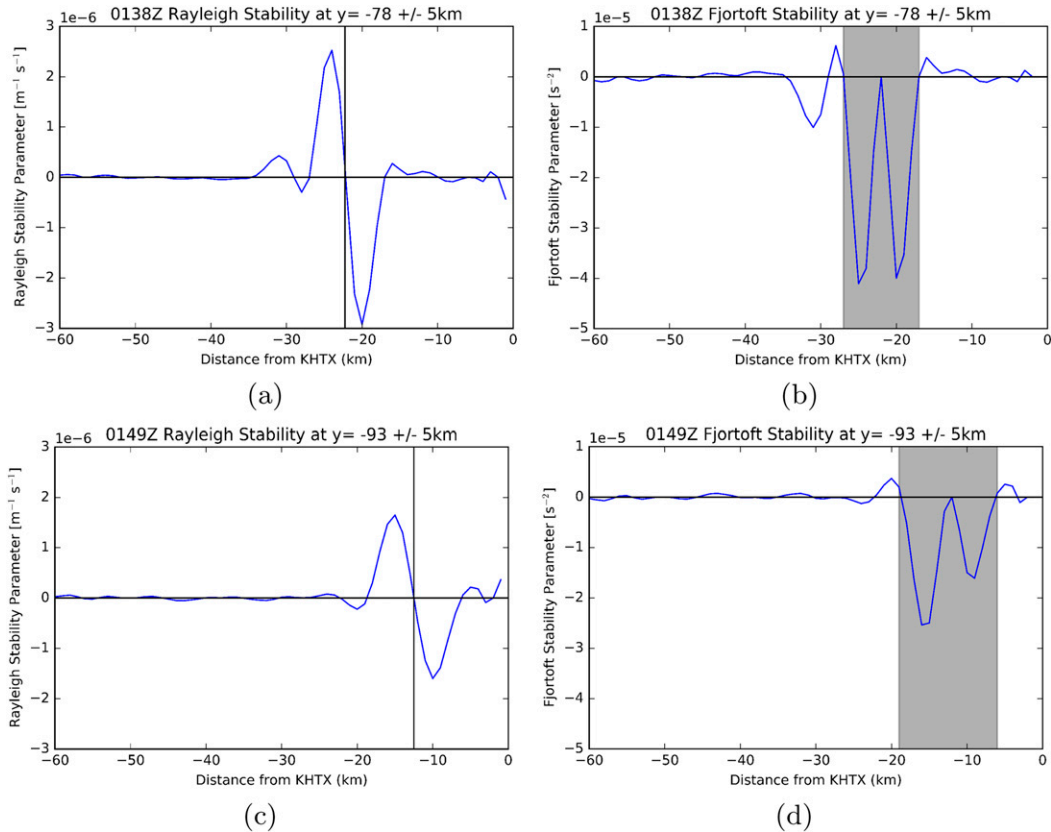
FIG. 8. Rayleigh and Fjørtoft criteria horizontal profiles in the east/west direction centered through the (a),(b) tornadic and (c),(d) nondamaging mesovortex at 1.5 km MSL (1.2 km AGL) for the 4 Jan 2015 QLCS. The horizontal black line on the Rayleigh profile represents the location of the inflection point. The shaded box on the Fjørtoft criterion highlights the negative spike meaning that the criterion has been met for instability.

is defined by a 1.5-hPa step increase in pressure, a slight decrease in temperature and dewpoint (within a rainfall rate of about $85\,mm\,h^{-1}$) around 0110 UTC, and a distinct wind shift (110°) and maximum wind gust ($11\,m\,s^{-1}$). The temperature reduction of 0.4°C within the first 10 min of the QLCS passage (horizontal scale of 9.6 km using a time–space conversion from the observed propagation speed), coupled with the sharp pressure increase of 1.5 hPa, indicates that the QLCS was likely propagating as a bore[3] (Blake et al. 2017), that is, a significant cold pool was not associated with the wind shift and thus baroclinic generation of horizontal vorticity along the wind shift would be small near the surface. Two mesovortices formed along the leading edge of the QLCS about 0.5 h after the passage over the MIPS at 0110 UTC. An EF-1 tornado [on the enhanced Fujita (EF) scale] associated with the northern mesovortex

produced a damage track near 10.3 km in length in Albertville, Alabama. The southern mesovortex was not surveyed;[4] however, no damage reports were received unlike the northern mesovortex, thus for this case it is assumed that no damage occurred with the southern mesovortex.

Figures 8a and 8b depict horizontal profiles of the Rayleigh and Fjørtoft instability criteria for the northern mesovortex at 0138 UTC near the time of mesovortex formation and within 4 min prior to tornadogenesis. An inflection point was present in the flow at the leading edge of the QLCS (near $x = -23\,km$) at 0138 UTC as indicated by the change in sign of the Rayleigh criterion. Inspection of the Fjørtoft criterion shows two negative spikes indicating that shearing instability may be present along the leading edge. The return to 0 in the Fjørtoft criterion marks the location of the inflection point at the leading edge ($x = -23$) where $\overline{v} = \overline{v}_I$.

---

[3] A bore is a hydraulic jump that propagates within a stable boundary layer that produces a semipermanent vertical displacement of the layer. Bores are identified in surface data as a step increase in pressure accompanied by a negligible change in temperature (Knupp 2006).

[4] The ground survey of the northern vortex was performed by UAH personnel.
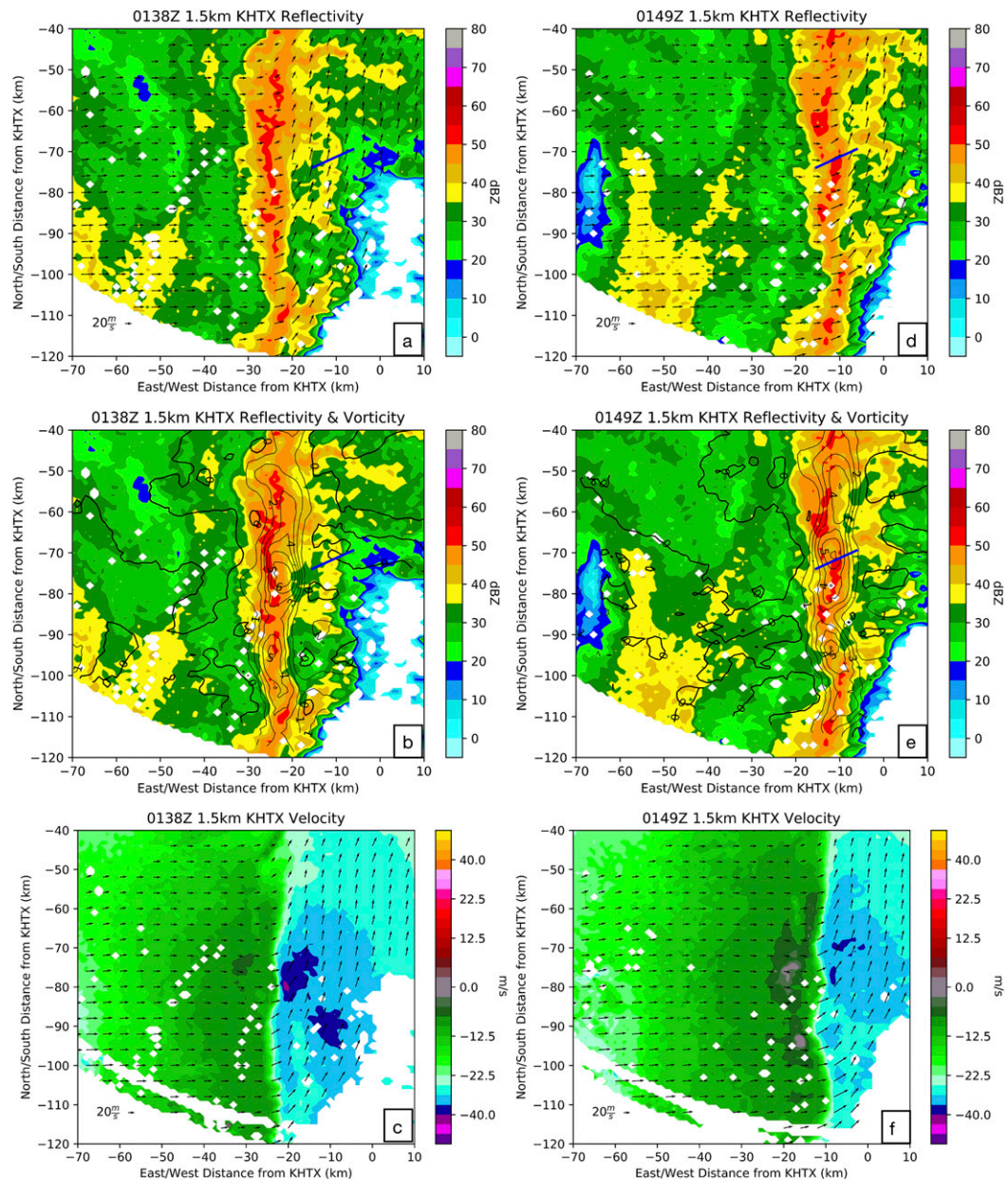
FIG. 9. Reflectivity with ground-relative winds, vertical vorticity ($1 \times 10^{-3}\,\mathrm{s}^{-1}$ contours), and KHTX radial velocity with ground-relative winds overlaid at (a)–(c) 0138 UTC and (d)–(f) 0149 UTC 4 Jan 2015 at 1.5 km MSL (1.2 km AGL). Negative values of vorticity have dashed contours. Bold in (b) and (e) shows the $0 \times 10^{-3}\,\mathrm{s}^{-1}$ contour. The blue line indicates the tornado damage track associated with the northern mesovortex.

A similar analysis was performed on the southern mesovortex at 0149 UTC (Figs. 8c,d). This time was selected as it is the last radar volume prior to the mesovortex reaching its peak intensity. As with the northern mesovortex, an inflection point was seen in the southern mesovortex at the leading edge of the QLCS ($x = -13\,\mathrm{km}$) at 0149 UTC. The Fjørtoft criterion was also met for the southern mesovortex as shown by the negative spikes in Fig. 8d.

Figure 9 depicts the horizontal wind field (Fig. 9a) and vertical vorticity (Fig. 9b) from the dual-Doppler analysis (lowest level of 1.5 km MSL, 1.2 km AGL) at the time of the peak vertical vorticity ($6 \times 10^{-3}\,\mathrm{s}^{-1}$) within the northern mesovortex at 0138 UTC. The blue line in all figure panels denotes the tornado damage track. A narrow region of continuous cyclonic vorticity (value near $3 \times 10^{-3}\,\mathrm{s}^{-1}$), which indicates where the region of greatest horizontal shear and thus the greatest
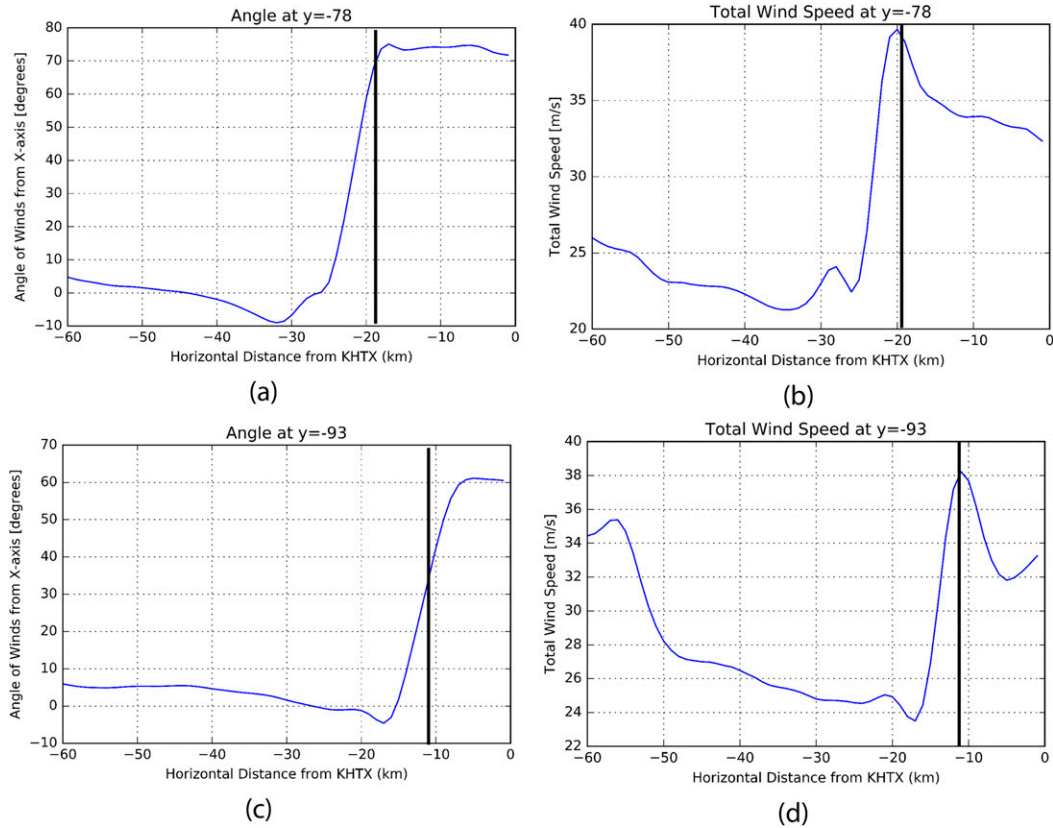
FIG. 10. Plots of 10-km horizontally averaged wind shift angle off of the x axis and wind speed in the east–west direction at 1.5 km MSL (1.2 km AGL) for the (a),(b) northern, tornadic mesovortex at 0138 UTC and (c),(d) southern, nondamaging mesovortex at 0149 UTC for the 4 Jan 2015 QLCS. Black vertical lines indicate the leading edge of the QLCS.

region of horizontal shearing instability, was present along the leading edge. Figures 9d and 9e show the same fields for 0149 UTC, when the southern mesovortex attained its peak intensity. The continuous vortex sheet was still present, with the cyclonic vorticity within the southern mesovortex around $5 \times 10^{-3} \, \mathrm{s}^{-1}$.

The overall magnitude of the wind speed and wind shift angle was determined, where θ denotes the angle between the wind vector and x axis. For example, for a wind direction of 275°, $\theta = -5°$; for a pure southerly wind, $\theta = 90°$. To remove the effects of the mesovortex, which has a horizontal scale of about 5 km, a 10-km meridional swath centered on each mesovortex was used with the northern mesovortex centered around $y = -78 \, \mathrm{km}$ and the southern mesovortex near $y = -93 \, \mathrm{km}$.

The magnitudes of the wind speed and the wind shift angle for the northern mesovortex at 0138 UTC are presented in Figs. 10a and 10b. Behind, at, and in front of the leading edge of the QLCS, wind speeds exceed $25 \, \mathrm{m \, s}^{-1}$ within 5 km zonally of the leading edge. A wind shift angle of almost 85° near the leading edge was also observed. Wind shift speed and angle plots for the

southern mesovortex are given in Figs. 10c and 10d. Strong winds of 24–$38 \, \mathrm{m \, s}^{-1}$ were located behind, at, and ahead of the leading edge of the QLCS in the zonal direction, however, the wind shift angle for the southern mesovortex was closer to 65°, which was 20° lower than the 85° associated with the northern mesovortex. These results agree with those presented in CP14, with the northern mesovortex falling into their tornadic classification (wind shift angle near 90°) and the southern mesovortex falling into their strong wind, but nontornadic classification, as its wind shift angle was near 65° rather than near 90°, which is apparently required to be in the tornadic category.

Further evidence that HSI is the primary formation mechanism of these mesovortices is agreement with linear theory, which predicts that for shearing instability, disturbances (vortices) that develop should have a wavelength of approximately 7.9 times the width of the shear zone (Buban and Ziegler 2016b). To estimate the width of the shear zone, the half-width of vertical vorticity was used. Within the tornadic mesovortex, the maximum vertical vorticity magnitude was
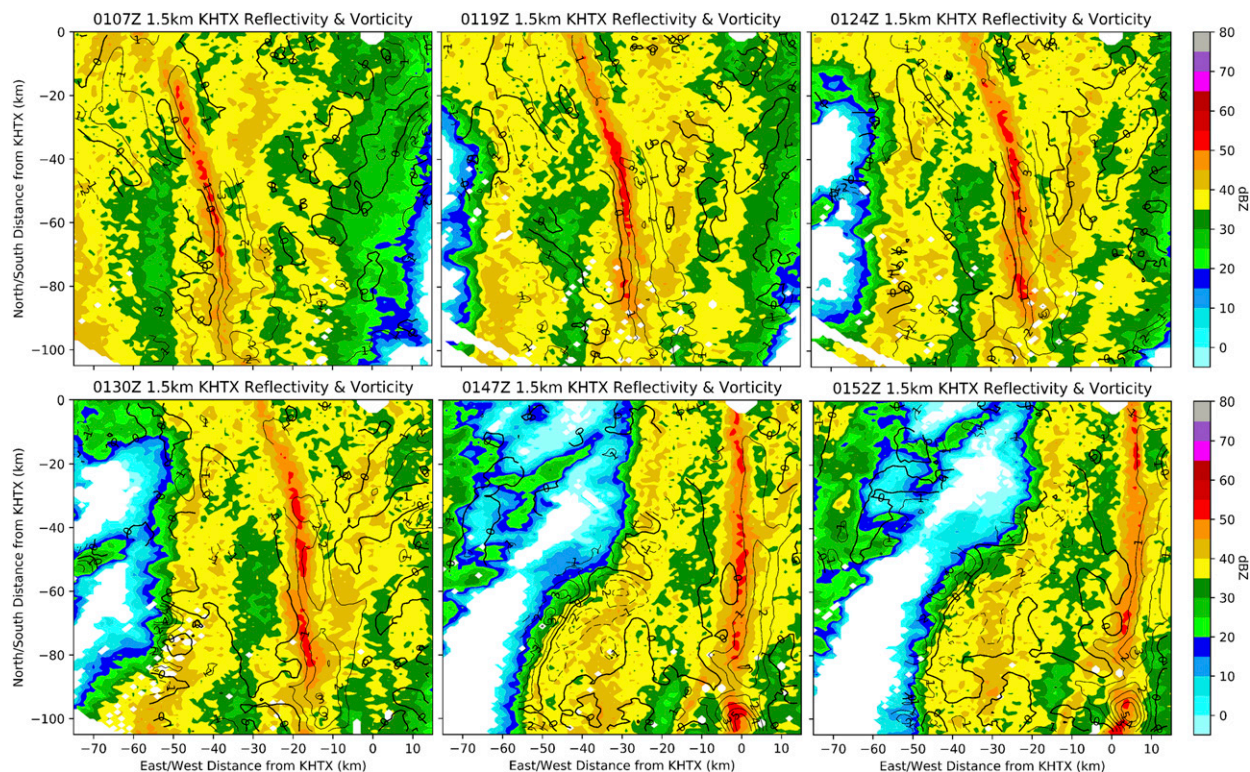
FIG. 11. Overview of 28 Nov 2016 QLCS at (a) 0107, (b) 0119, (c) 0124, (d) 0130, (e) 0147, and (f) 0152 UTC following an 18° rotation; reflectivity from KHTX with vertical vorticity ($1 \times 10^{-3}\,\mathrm{s}^{-1}$ contours). Negative values of vorticity have dashed contours. Bold shows the $0 \times 10^{-3}\,\mathrm{s}^{-1}$ contour. Location of the surface data and UAH is near ($x = -58$, $y = -32$).

approximately $6.5 \times 10^{-3}\,\mathrm{s}^{-1}$. Thus, the shear zone width was defined by the zonal width between the $3.25 \times 10^{-3}\,\mathrm{s}^{-1}$ vertical vorticity contours along the leading edge of the QLCS. The estimated shear zone width outside the regions of the mesovortices was approximately 2–3 km, which yields a wavelength between 15.8 and 23.7 km. Using the centers of the vertical vorticity maxima associated with each mesovortex, the distance between the two vortices was about 17.5 km, within the range predicted by the linear theory of shearing instability. Additionally, Batchelor (2000) showed that for instabilities produced at a shearing interface, the shear zone width increased near the disturbances and decreased in between. This pattern was observed in the vertical vorticity field of Fig. 9, with the $3.25 \times 10^{-3}\,\mathrm{s}^{-1}$ contour wider at the location of the vortices and narrower in-between.

Although tilting of locally generated horizontal vorticity could not be resolved on a sufficiently fine-scale due to the ARMOR scan strategy and the 70-km baseline between the two radars, it is hypothesized that the tilting processes considered in other studies on the theory of mesovortexgenesis in QLCSs (TW03; WT03; AL09a,b) did not occur here. Since this QLCS was

likely propagating as a bore, a strong baroclinic zone along the leading edge of the QLCS, which TW03 showed could be tilted downward by a convective-scale downdraft, was not apparent. Additionally, the absence of a strong RIJ responsible for the generation of horizontal vorticity that would be tilted downward during the mature stage of the QLCS, as shown in TW03 and WT03, was not observed in this QLCS. The upward tilting of preexisting horizontal vorticity generated by the cross-gust-front baroclinic zone caused by a surge in the leading edge of the QLCS (AL09a,b's second mechanism) is also not likely, as no surges were observed, nor was a baroclinic zone indicated by surface data. Moreover, these three theories predict the formation of mesovortex couplets (cyclonic/anticyclonic) which was not observed in this QLCS (Figs. 9c,f). The first mechanism discussed in AL09a,b is also not likely as it relies on the generation of horizontal vorticity by a baroclinic zone that was not apparent in this case.

b. 28 November 2016 (null case)

On 28 November 2016, a QLCS traversed across the northern Alabama mesoscale domain between 0050
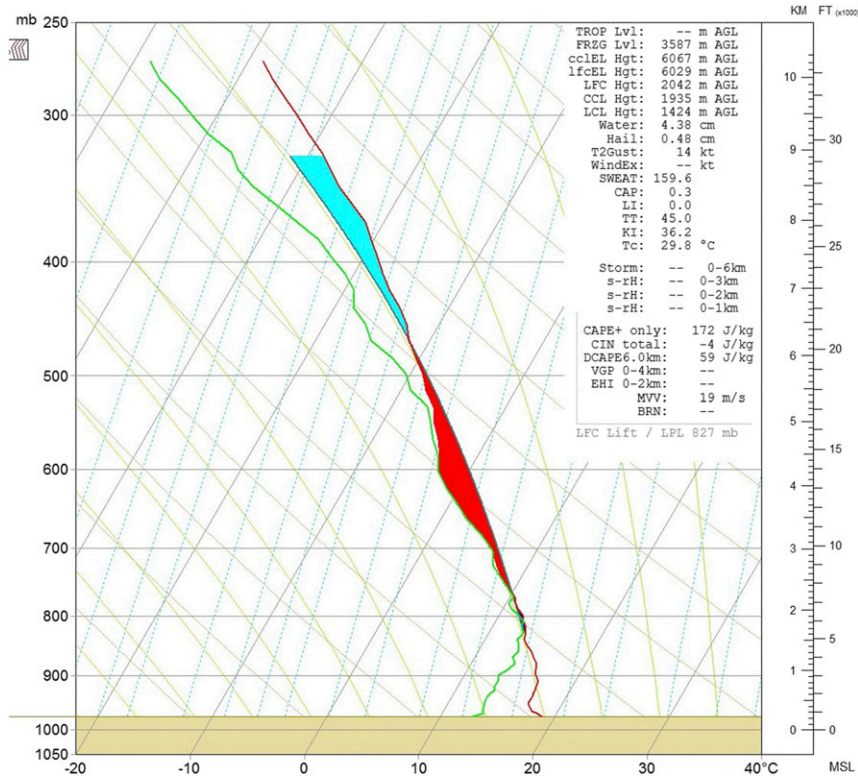
FIG. 12. Sounding at 0023 UTC 28 Nov 2016 near Huntsville, AL, from the RaDAPS MPR. Red (green) line is temperature (dewpoint) in °C. Black line indicates parcel temperature, while red shading is positive buoyant energy and blue is negative buoyant energy.

and 0150 UTC (Fig. 11). There were no severe hail or tornado reports associated with the QLCS; it is highly unlikely that severe weather occurred given that the QLCS passed over a relatively populated area. The environment over north Alabama exhibited HSLC characteristics with estimated 172 J kg^{-1} most-unstable CAPE[5] (Fig. 12). Evidence of evaporative cooling from the leading stratiform precipitation was observed starting at 0010 UTC in the time series of temperature and dewpoint temperature (Fig. 13), with a 4-K decrease in the equivalent potential temperature (not shown). Storm Prediction Center mesoanalysis (https://www.spc.noaa.gov/exper/mesoanalysis/) depicted near 41 m s^{-1} of 0–6-km bulk wind shear. Figure 14 depicts a time–height section of the 0–4-km wind profiles from the RaDAPS 915-MHz wind profiler located at the SWIRLL facility. A veering wind profile with height was observed with 25 m s^{-1} of bulk shear in the 0–4-km layer from 2200 to 2400 UTC. As the QLCS approached, the 0–4-km bulk shear increased to near 30 m s^{-1} within the leading

stratiform precipitation (from 0000 to 0100 UTC, hour 24 to 25). An increase of the midlevel wind speeds of about 15 m s^{-1} near 4 km AGL was also seen at hour 25 (0100 UTC).

The QLCS had a forward propagating speed near 20 m s^{-1}. Time series of surface parameters show that at the arrival of the QLCS convective region (0110 UTC), a rapid pressure rise of 2.5 hPa, a temporary wind shift from the west, and a 0.5°C temperature drop during the first 10 min of the QLCS passage (12-km horizontal scale) indicate that the QLCS was likely propagating as a solitary wave.[6] Thus, baroclinic effects not likely significant, as in the 4 January 2015 case due to the absence of a cold pool.

Since no mesovortices formed within this QLCS, profiles of the change of wind speed, wind shift angle, and instability criteria were taken at different locations

---

[5] In situ thermodynamic characteristics of the storm inflow are not available due to radiosonde measurements 2 h prior to QLCS arrival; however, it showed characteristics of HSLC environments.

[6] A solitary wave is a buoyancy wave that propagates within a stable layer. Surface data exhibit a pressure increase and subsequent decrease (consistent with air rising and then sinking in a stable atmosphere), and temperature exhibits a negligible change (Knupp 2006). Unlike bores, solitary waves do not produce a sustained lifting of atmospheric layers.
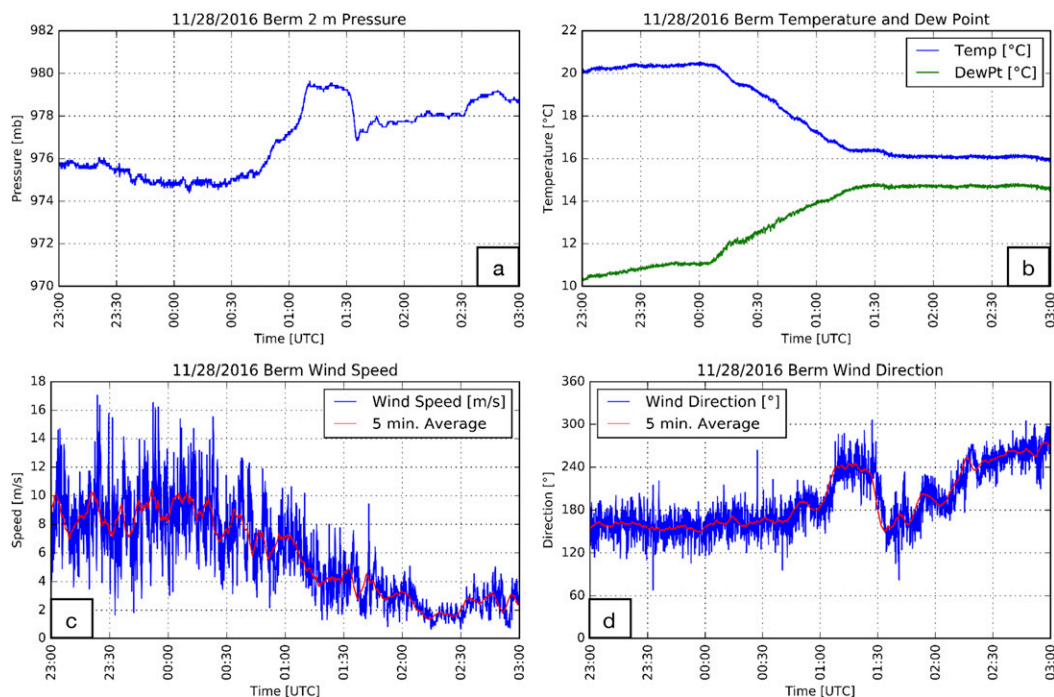
FIG. 13. Traces of (a) 2-m pressure, (b) 2-m temperature/dewpoint, (c) 10-m wind speed, and (d) 10-m wind direction from the UAH SWIRLL facility (berm). QLCS passage over instrumentation occurred shortly after 0100 UTC. The RH sensor has a low bias that is estimated to lead to a 1°C low bias in the derived dewpoint; the air 0115 UTC onward is likely close to saturation.

along the leading edge at about 20-min intervals to sample different parts of the wind shift. The QLCS developed an echo top of about 8 km and an average updraft, as determined from the dual-Doppler synthesis, of less than $5 \, m \, s^{-1}$ (not shown). The absence of lightning supports the low value of the dual-Doppler-estimated updraft magnitudes with this QLCS (Fig. 6b; Deierling and Petersen 2008). Since extensive stratiform precipitation preceded the convective line, it was likely that evaporative cooling played a role in the increase of low-level stability.

Rayleigh instability criterion profiles at different locations of the QLCS at 0107, 0124, and 0147 UTC are given in Fig. 15. As with the 4 January 2015 QLCS, the winds are averaged over a 10-km meridional swath to smooth out local variability along the leading edge. At all times, the Rayleigh criterion changes sign at the leading edge of the QLCS. However, it is difficult to discern if the change in sign is due to the presence of an inflection point or base state variability. The major difference between this QLCS and the 4 January 2015 QLCS is that the change in sign for both the northern and southern vortices for the 4 January 2015 QLCS stands out sharply whereas for the 28 November 2016 QLCS, the change was more subtle at most times as the values of both criteria at the leading edge of the QLCS

are not significantly larger than the values along the profile in regions displaced from the leading edge of the QLCS.

Fjørtoft profiles at the same times and locations as the Rayleigh profiles are displayed in Fig. 16. As with the Rayleigh profiles, the negative values associated with the inflection point of the Fjørtoft criterion are difficult to discern from the base state variability. For all the times presented, the Fjørtoft criterion has negative values near the leading edge. Although all the times presented show negative values, the Fjørtoft criterion was only met at 0124 and 0147 UTC. At 0107 UTC, the Fjørtoft criterion was not met as the negative spike is ahead (east) of the inflection point whereas with the other times and events, the inflection point was either within or close to the middle of the minimum. Although the Rayleigh and Fjørtoft criteria were met during certain times in which a dual-Doppler analysis was possible, mesovortices did not form along the leading edge of the QLCS. This highlights a limitation of using the Rayleigh and Fjørtoft criteria alone to determine if HSI is a plausible mechanism of mesovortexgenesis.

The horizontal wind field and vertical vorticity from the dual-Doppler retrievals are given in Fig. 17. A wind shift was present along the leading edge of the QLCS
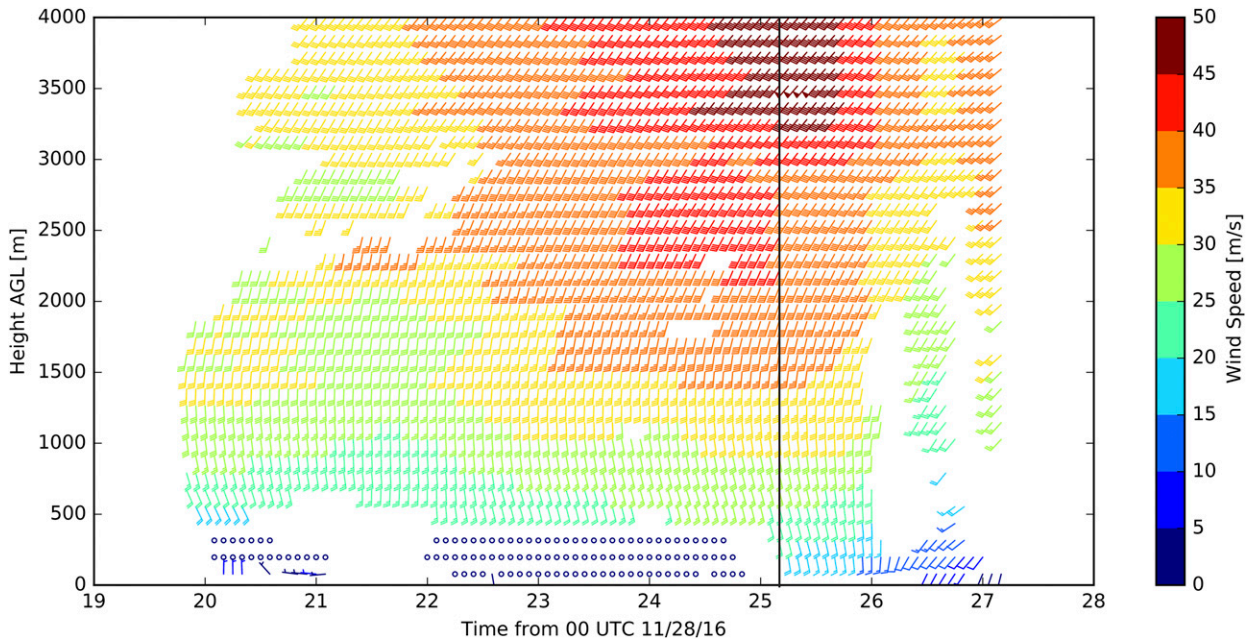
FIG. 14. Vertical wind profiles with 5-min sampling from the RaDAPS 915-MHz wind profiler located at the UAH SWIRLL facility. Wind barbs are speed in m s^{-1}. Black, vertical line represents time of QLCS convective region passage. Bulk wind shear in the 0–4-km layer immediately prior to the QLCS arrival is near 25 m s^{-1}.

convective region as it traversed through the dual-Doppler domain and sharpened during this time frame. The reflectivity factor within the precipitation core increased as the wind shift became sharper. A line of positive vertical vorticity, with a magnitude of vertical vorticity around $2 \times 10^{-3} \text{s}^{-1}$ and small pockets of vorticity reaching values near $3.5 \times 10^{-3} \text{s}^{-1}$, is also present at the leading edge of the QLCS. This indirectly reveals the region of greatest horizontal shear, and thus the greatest region of horizontal shearing instability. In comparison with the 4 January 2015 QLCS, the wind shift was not as sharp and the peak value of vorticity within the maximum axis was $2 \times 10^{-3} \text{s}^{-1}$ less in the 28 November 2016 case than in the 4 January 2015 case. The 4 January 2015 QLCS also developed more pockets of stronger vorticity, with peak values reaching $3.5 \times 10^{-3} \text{s}^{-1}$ outside of the two vortices.

The change in the wind speed and wind shift angle is shown in Fig. 18 and Fig. 19, with θ being the angle of the wind from of the x axis. For the times and locations depicted in Fig. 18, the change of wind speed behind, at, and in front of the leading edge of the QLCS in the zonal direction was about 15 m s^{-1}, with a gradual increase from behind through ahead of the

[7] This terminology is used to be consistent with the results of the CP14 study.

QLCS rather than strong winds[7] behind, at, and ahead of the leading edge. The wind shift angles (around 60°) shown in Fig. 19 display a lack of a pronounced wind shift (close to 90°), consistent with the findings of CP14 which showed that a weak wind shift (much less than 90°) was not conducive for tornadoes. The combination of a weak wind shift angle and the gradual increase of the wind speeds on the back side of the leading edge of the QLCS was not conducive for the formation of tornadoes (and thus mesovortices) in this event. This was most notably seen in the weaker magnitude of the vertical vorticity at the leading edge of the 28 November 2016 QLCS. This is further supported by the 10-m wind speed and direction (Fig. 13), as there is only about a 60° change in the wind direction associated with the QLCS passage along with a small (4 m s^{-1}) change in wind speed, implying less convergence and weaker updrafts at the leading edge of the QLCS.

4. Summary and conclusions

This study investigated the role that HSI played in the formation of two mesovortices in one QLCS and the lack of mesovortices in another, both of which were propagating as a wave-like feature (bore or solitary wave) which implies the lack of a strong density current with a baroclinic leading edge. A dual-Doppler analysis was
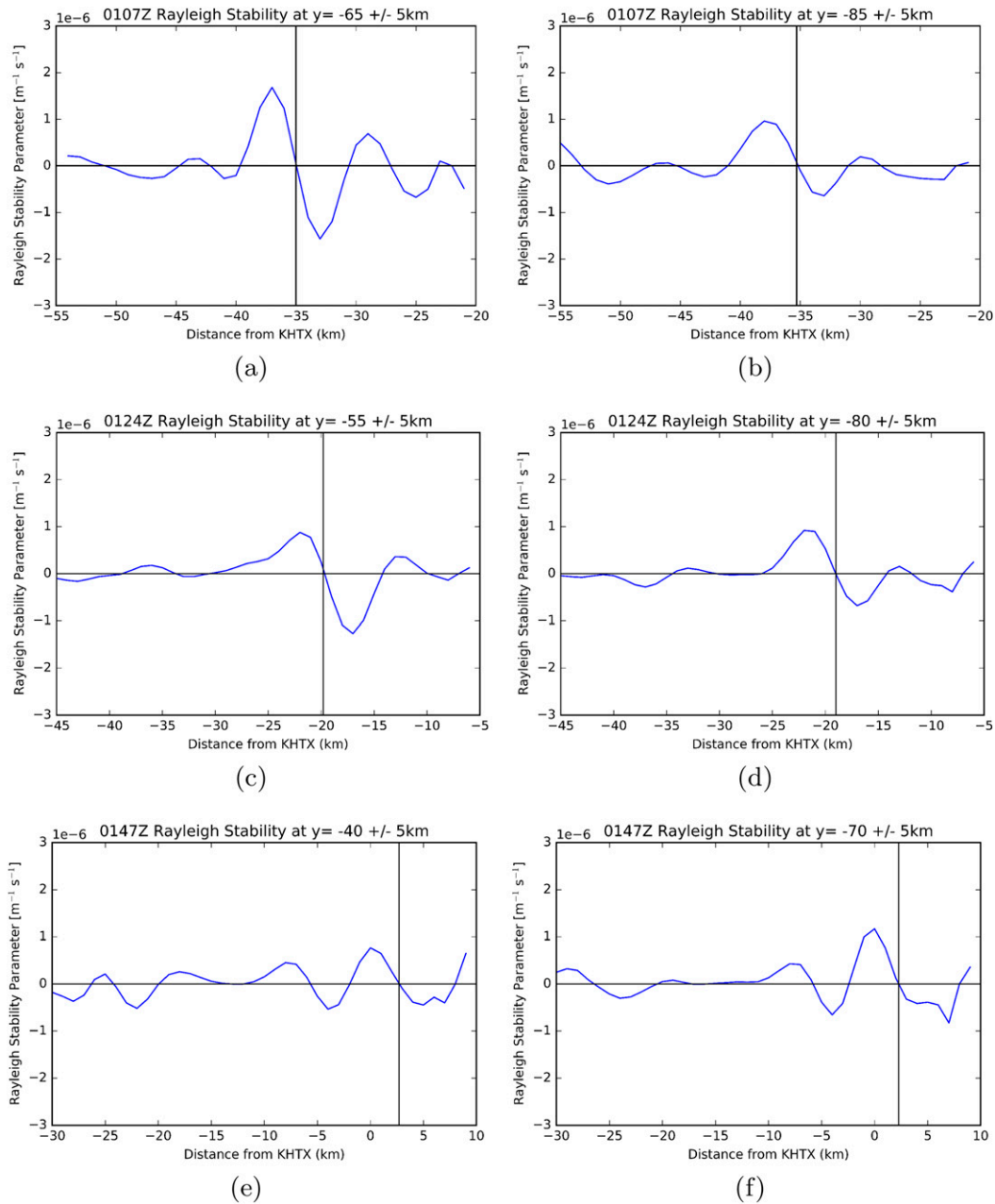
FIG. 15. Horizontal profiles in the east/west direction of the Rayleigh instability criterion for the 28 Nov 2016 QLCS. Vertical black line represents the leading edge of the QLCS.

performed for both events that occurred in HSLC environments.

The 4 January 2015 QLCS was a bore-propagating tornadic QLCS, which has not been documented previously from an observational or numerical simulation perspective. Prior to entering the dual-Doppler domain and the analysis time period, the vertical bulk shear ahead of the QLCS ($25\,\mathrm{m\,s^{-1}}$ at 1.2 km AGL from dual-Doppler winds, $4\,\mathrm{m\,s^{-1}}$ surface wind speed), likely

created environmental horizontal vorticity that would be tilted upward to produce the vertical vortex sheet by convergence at the leading edge of the QLCS. Following the formation of the vertical vortex sheet, HSI was shown to be a significant formation mechanism of the two mesovortices. This process was alluded to in a modeled cold-season QLCS examined by Wheatley and Trapp (2008). The Rayleigh and Fjørtoft instability criteria are met for the shear zone of both vortices.
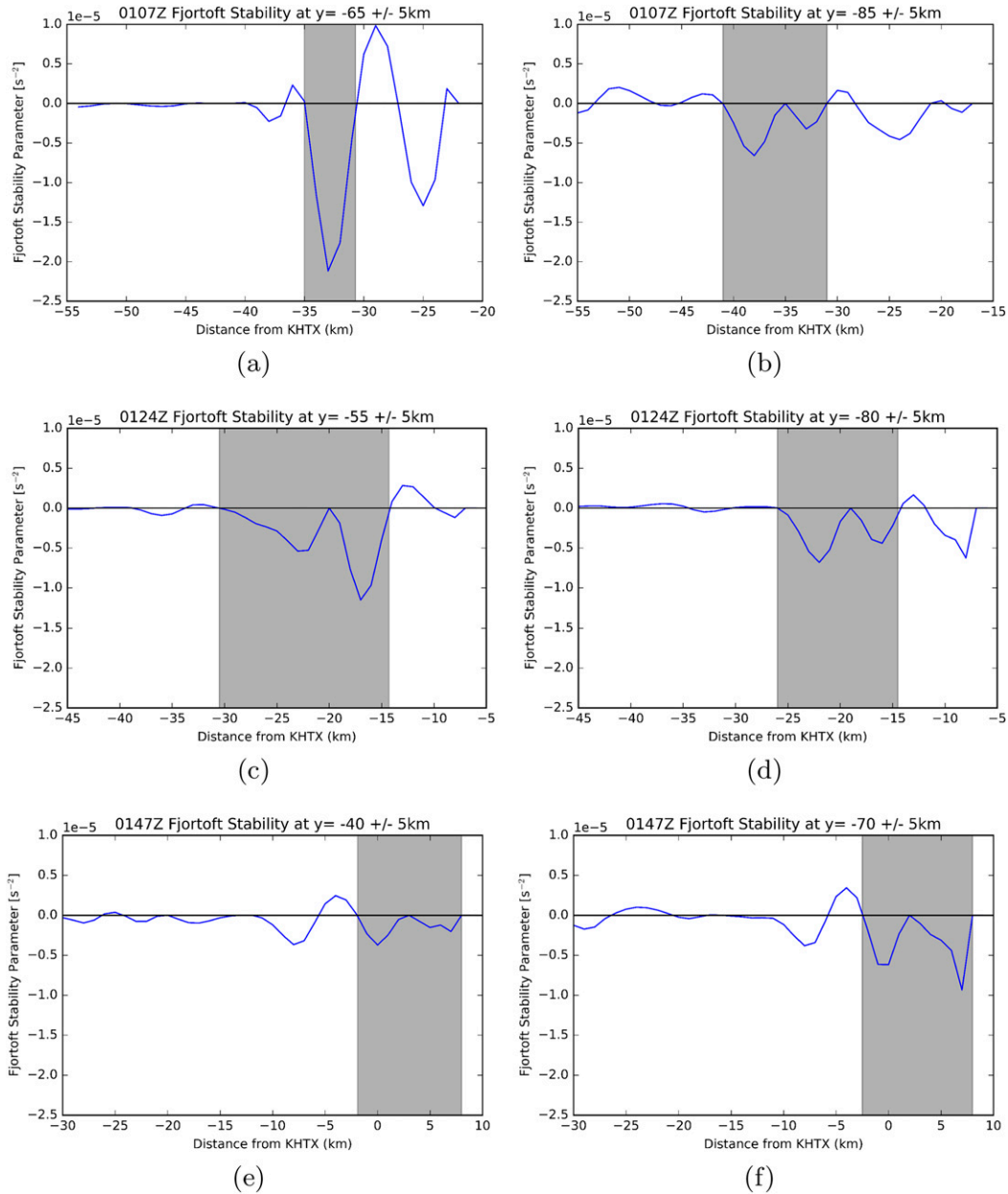
FIG. 16. Horizontal profiles in the east/west direction of the Fjørtoft instability criterion for the 28 Nov 2016 QLCS. The shaded box on the Fjørtoft criterion highlights the negative spike meaning that the criterion has been met for instability.

The results found here are also in agreement with the results presented in CP14 with strong winds behind and ahead of the QLCS, a distinct maximum in wind speed near the leading edge of the QLCS and a sharp wind shift angle. For the tornadic mesovortex, a wind shift angle of almost 90° and strong winds surrounding the leading edge were diagnosed. For the nondamaging southern mesovortex, a weaker wind shift near 65° was observed. Additionally, only positive, continuous vertical

vorticity was analyzed along the leading edge of the QLCS while it moved through the dual-Doppler domain. Despite the height limitations of the dual-Doppler analysis (1.2 km AGL), the values of the instability criteria are still robust. It is expected that as the analysis height approaches the surface, the instability criteria values would increase as the wind shift gradient becomes more pronounced near the surface. This is seen in the time series of the 10-m wind direction (Fig. 7) as the wind
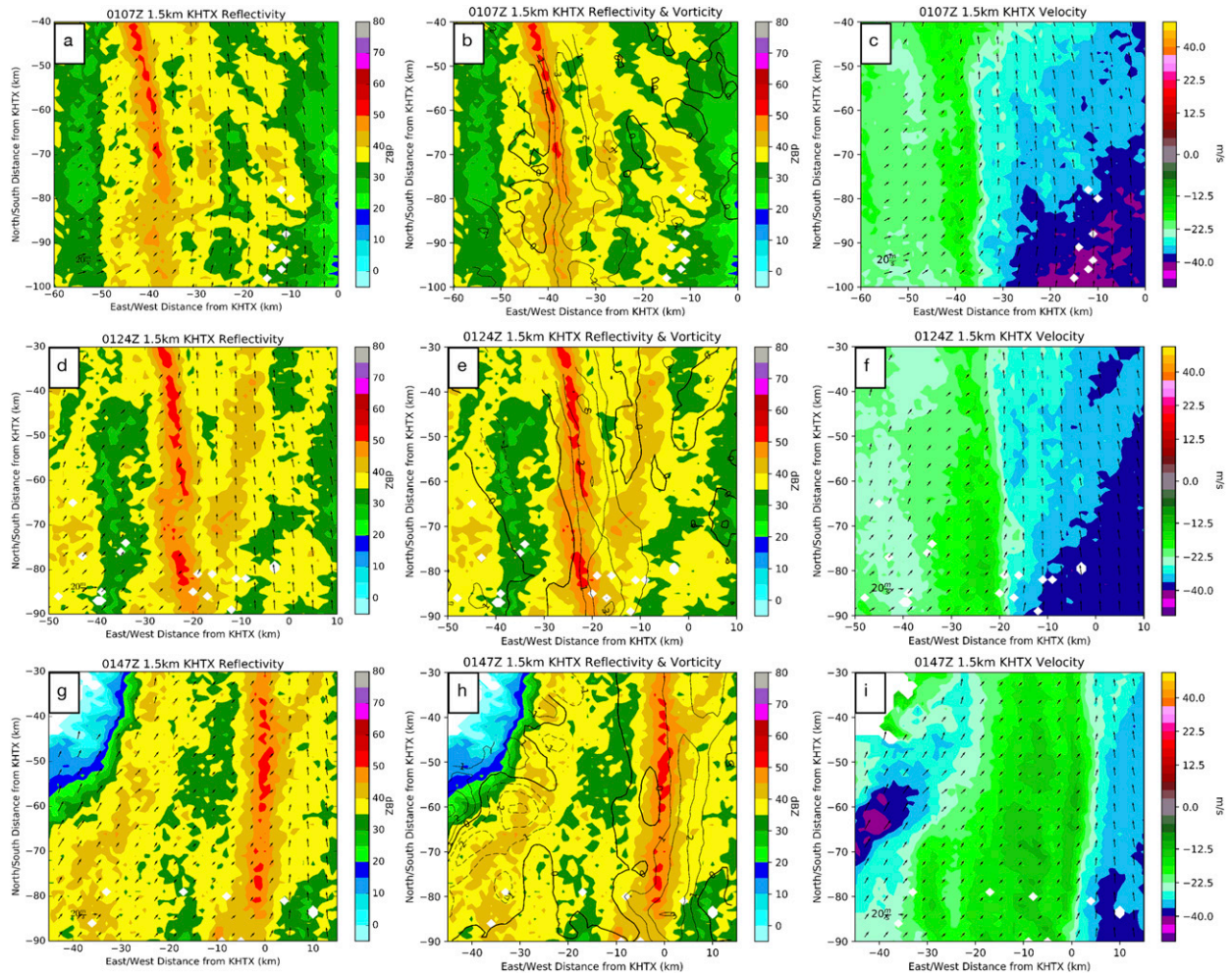
FIG. 17. Reflectivity from KHTX with horizontal dual-Doppler winds, vertical vorticity ($1 \times 10^{-3}\,\text{s}^{-1}$ contours; positive values solid, negative values dashed), and KHTX radial velocity with ground-relative winds at (a)–(c) 0107, (d)–(f) 0124, and (g)–(i) 0147 UTC 28 Nov 2016. Bold shows the $0 \times 10^{-3}\,\text{s}^{-1}$ contour.

direction changes from 180° ahead of the QLCS to 290° within several minutes of passage. This shows that the wind shift is indeed larger at the surface than what is seen in the much lower-resolution dual-Doppler analysis at 1.2 km AGL.[8]

The results for the 28 November 2016 QLCS agree with the results presented in CP14. The wind shift associated with this QLCS was more broad, which is consistent with a lower value of the wind shift gradient (less convergence) when compared to the 4 January 2015 event. The overall wind speed also showed a broad increase from behind through the leading edge rather than being strong behind and in

front of the leading edge along with a broader wind shift near 60°, less than the near 90° wind veer of the tornadic category. These characteristics would place this QLCS in the "nontornadic" category consistent with the results presented in CP14. Satisfaction of the Rayleigh criterion was not conclusive as the change in sign was not strong enough to be discerned over the background mesoscale variability. The Fjørtoft instability criterion was only met for four out of the six analysis times for the 28 November 2016 QLCS. According to the Rayleigh and Fjørtoft instability criteria, mesovortices should have also formed in the 28 November 2016 QLCS, but none were observed. This highlights the drawback of using required, but insufficient criteria and why the results of the CP14 study are included in this analysis. Other proxies that characterize the updraft strength, such as the echo

---

[8] A direct comparison to between the surface time series and dual-Doppler analysis cannot be made though because of the differing spatial resolutions.
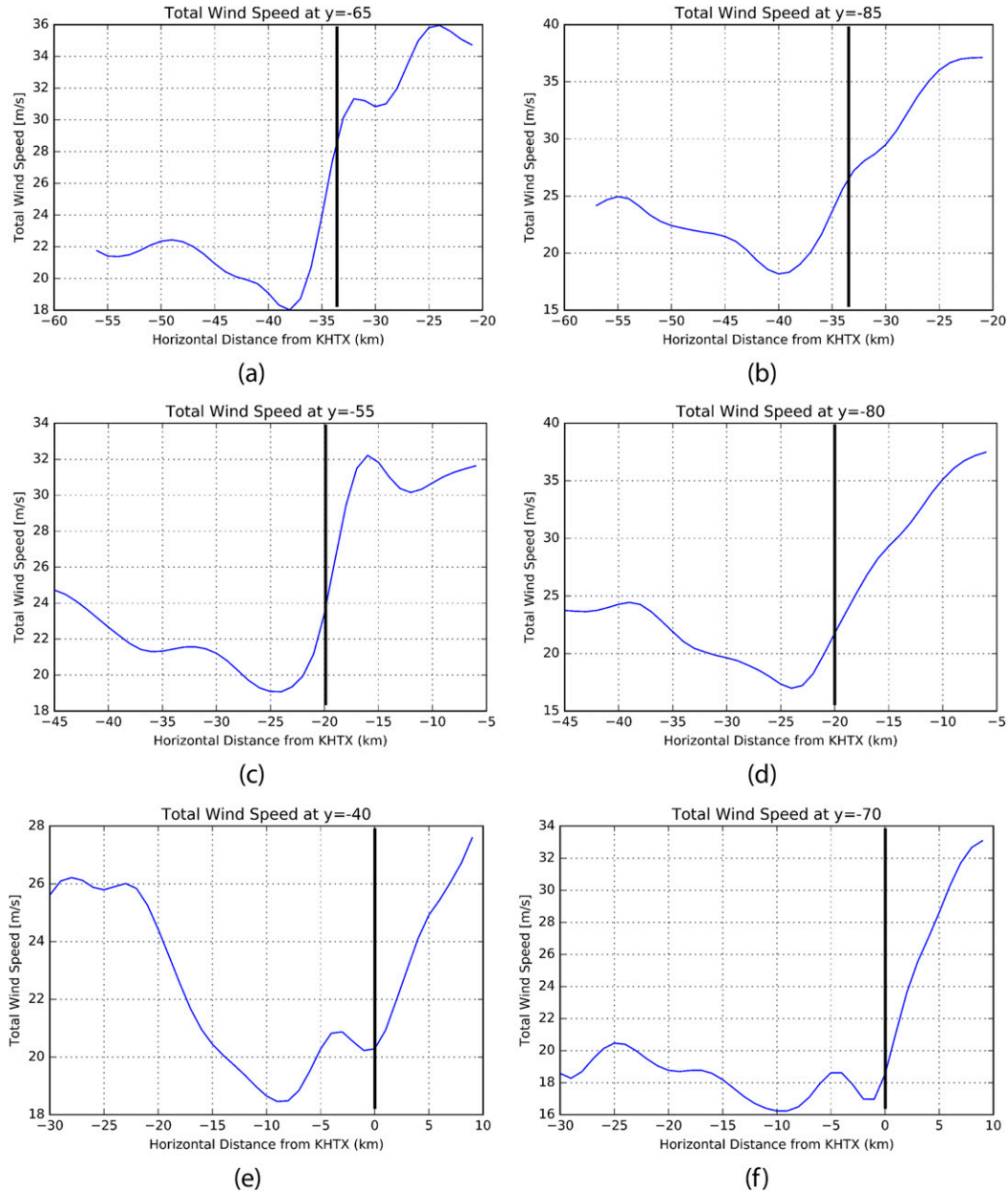
FIG. 18. Wind speed centered at different locations along the leading edge of the QLCS at 1.5 km MSL (1.2 km AGL) in the east/west direction at (a),(b) 0107, (c),(d) 0124, and (e),(f) 0147 UTC for the 28 Nov 2016 QLCS. Black vertical lines indicate the leading edge of the QLCS.

top height, the height of the 40-dBZ reflectivity contour, occurrence of the 2σ lightning jump (Schultz et al. 2009), and the presence of Z_{DR} columns (all of which are related to updraft intensity) may also prove useful to identifying the likelihood or location of mesovortexgenesis.

Given the lack of cyclonic/anticyclonic vortex couplets, a strong RIJ, a surging segment, or a density current in both events, it is unlikely that the other theories of mesovortexgenesis were applicable in these two

cases. Most notably, the lack of a strong density current due to the propagation mechanism (bore or solitary wave) implies that the baroclinic horizontal vorticity generated along the leading edge of the QLCS, shown to be vital in the current theories, was not required for the formation of vortices in the 4 January 2015 QLCS. This study investigates the potential for another mechanism of mesovortexgenesis in QLCSs, particularly in QLCSs that occur in HSLC environments. For the 4 January 2015 QLCS analyzed here, it is demonstrated that
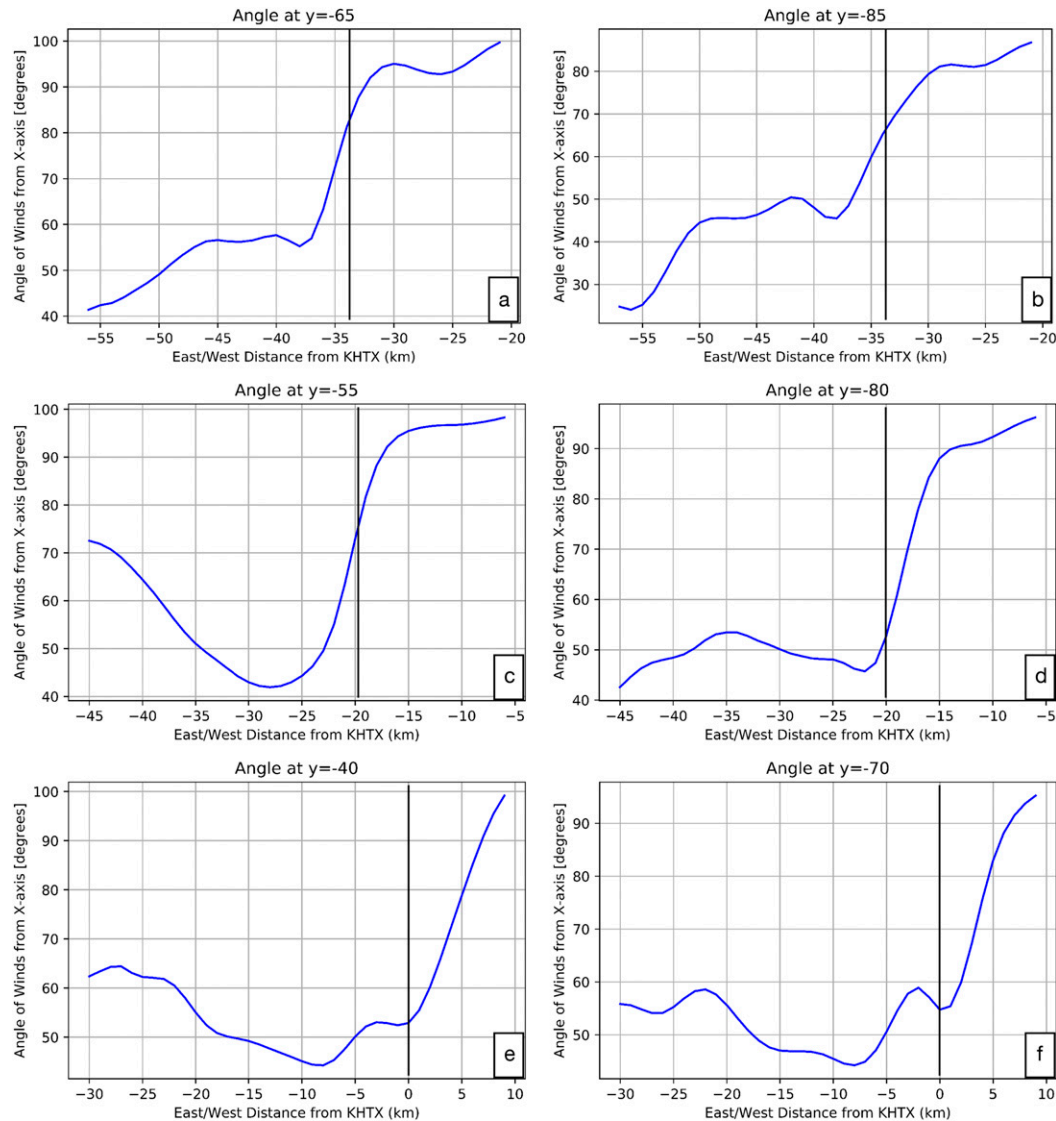
FIG. 19. Wind shift angle profiles centered at the same locations as in Fig. 18 at 1.5 km MSL (1.2 km AGL) in the east/west direction at (a),(b) 0107, (c),(d) 0124, and (e),(f) 0147 UTC for the 28 Nov 2016 QLCS. Black vertical lines indicate the leading edge of the QLCS.

HSI was the likely formation mechanism given that the instability criteria were satisfied and the lack of the defining features noted in the other aforementioned mesovortexgenesis theories.

Future work will include collecting and analyzing data on more events with improved radar coverage and spatial resolution, at low levels in particular, and in situ observations. Changes in boundary layer wind profiles and thermodynamics sampled by profiling instrumentation will be used to determine how wind profiles vary along the leading edge of the QLCS and the effects of stability on mesovortexgenesis potential. Observations will target not only QLCSs in HSLC environments, but ones in environments with varying wind and thermodynamic profiles in an attempt to observe mesovortices along the leading edge.

REFERENCES

Arnott, N., Y. Richardson, J. Wurman, and E. Rasmussen, 2006: Relationship between a weakening cold front, misocyclones, and cloud development on 10 June 2002 during IHOP. *Mon. Wea. Rev.*, **134**, 311–335, https://doi.org/10.1175/MWR3065.1.

Atkins, N. T., and M. S. Laurent, 2009a: Bow echo mesovortices. Part I: Processes that influence their damaging potential. *Mon. Wea. Rev.*, **137**, 1497–1513, https://doi.org/10.1175/2008MWR2649.1.

——, and ——, 2009b: Bow echo mesovortices. Part II: Their genesis. *Mon. Wea. Rev.*, **137**, 1514–1532, https://doi.org/10.1175/2008MWR2650.1.

——, R. M. Wakimoto, and C. L. Ziegler, 1998: Observations of the finescale structure of a dryline during VORTEX 95. *Mon. Wea. Rev.*, **126**, 525–550, https://doi.org/10.1175/1520-0493(1998)126<0525:OOTFSO>2.0.CO;2.

Batchelor, G. K., 2000: *An Introduction to Fluid Dynamics.* Cambridge University Press, 658 pp., https://doi.org/10.1017/CBO9780511800955.

Bell, M. M., W. C. Lee, C. A. Wolff, and H. Cai, 2013: A solo-based automated quality control algorithm for airborne tail Doppler radar data. *J. Appl. Meteor. Climatol.*, **52**, 2509–2528, https://doi.org/10.1175/JAMC-D-12-0283.1.

Blake, B. T., D. B. Parsons, K. R. Haghi, and S. G. Castleberry, 2017: The structure, evolution, and dynamics of a nocturnal convective system simulated using the WRF-ARW Model. *Mon. Wea. Rev.*, **145**, 3179–3201, https://doi.org/10.1175/MWR-D-16-0360.1.

Buban, M. S., and C. L. Ziegler, 2016a: The formation of small-scale atmospheric vortices via baroclinic horizontal shearing instability. *J. Atmos. Sci.*, **73**, 2085–2104, https://doi.org/10.1175/JAS-D-14-0385.1.

——, and ——, 2016b: The formation of small-scale atmospheric vortices via horizontal shearing instability. *J. Atmos. Sci.*, **73**, 2061–2084, https://doi.org/10.1175/JAS-D-14-0355.1.

——, ——, E. R. Mansell, and Y. Richardson, 2012: Simulation of dryline misovortex dynamics and cumulus formation. *Mon. Wea. Rev.*, **140**, 3525–3551, https://doi.org/10.1175/MWR-D-11-00189.1.

Carbone, R. E., 1982: A severe frontal rainband. Part I: Stormwide hydrodynamic structure. *J. Atmos. Sci.*, **39**, 258–279, https://doi.org/10.1175/1520-0469(1982)039<0258:ASFRPI>2.0.CO;2.

——, 1983: A severe frontal rainband. Part II: Tornado parent vortex circulation. *J. Atmos. Sci.*, **40**, 2639–2654, https://doi.org/10.1175/1520-0469(1983)040<2639:ASFRPI>2.0.CO;2.

Chong, M., J. Testud, and F. Roux, 1983: Three-dimensional wind field analysis from dual-Doppler radar data. Part II: Minimizing the error due to temporal variation. *J. Climate Appl. Meteor.*, **22**, 1216–1226, https://doi.org/10.1175/1520-0450(1983)022<1216:TDWFAF>2.0.CO;2.

Clark, M. R., and D. J. Parker, 2014: On the mesoscale structure of surface wind and pressure fields near tornadic and nontornadic cold fronts. *Mon. Wea. Rev.*, **142**, 3560–3585, https://doi.org/10.1175/MWR-D-13-00395.1.

Davies-Jones, R., 1979: Dual-Doppler radar coverage area as a function of measurement accuracy and spatial resolution. *J. Appl. Meteor.*, **18**, 1229–1233, https://doi.org/10.1175/1520-0450-18.9.1229.

Davis, J. M., and M. D. Parker, 2014: Radar climatology of tornadic and nontornadic vortices in high-shear, low-CAPE environments in the mid-Atlantic and southeastern United States. *Wea. Forecasting*, **29**, 828–853, https://doi.org/10.1175/WAF-D-13-00127.1.

Deierling, W., and W. A. Petersen, 2008: Total lightning activity as an indicator of updraft characteristics. *J. Geophys. Res.*, **113**, D16210, https://doi.org/10.1029/2007JD009598.

Dixon, M., and G. Wiener, 1993: TITAN: Thunderstorm Identification, Tracking, Analysis, and Nowcasting—A radar-based methodology. *J. Atmos. Oceanic Technol.*, **10**, 785–797, https://doi.org/10.1175/1520-0426(1993)010<0785:TTITAA>2.0.CO;2.

Doviak, R. J., and D. S. Zrnić, 1993: *Doppler Radar and Weather Observations.* 2nd ed. Academic Press, 562 pp.

——, P. S. Ray, R. G. Strauch, and L. J. Miller, 1976: Error estimation in wind fields derived from dual-Doppler radar measurement. *J. Appl. Meteor.*, **15**, 868–878, https://doi.org/10.1175/1520-0450(1976)015<0868:EEIWFD>2.0.CO;2.

Drazin, P., and L. Howard, 1966: Hydrodynamic stability of parallel flow of inviscid fluid. *Adv. Appl. Mech.*, **9**, 1–89, https://doi.org/10.1016/S0065-2156(08)70066-1.

Fjørtoft, R., 1950: Application of integral theorems in deriving criteria of stability for laminar flows and for the baroclinic circular vortex. *Geofys. Publ.*, **17** (6), 52 pp.

Forbes, G. S., and R. M. Wakimoto, 1983: A concentrated outbreak of tornadoes, downbursts and microbursts, and implications regarding vortex classification. *Mon. Wea. Rev.*, **111**, 220–235, https://doi.org/10.1175/1520-0493(1983)111<0220:ACOOTD>2.0.CO;2.

Guyer, J., and A. Dean, 2010: Tornadoes within weak CAPE environments across the continental United States. *25th Conf. on Severe Local Storms*, Denver, CO, Amer. Meteor. Soc., 1.5, https://ams.confex.com/ams/25SLS/techprogram/paper_175725.htm.

Haurwitz, B., 1949: The instability of wind discontinuities and shear zones in planetary atmospheres. *J. Meteor.*, **6**, 200–206, https://doi.org/10.1175/1520-0469(1949)006<0200:TIOWDA>2.0.CO;2.

James, R. P., J. M. Fritsch, and P. Markowski, 2005: Environmental distinctions between cellular and slabular convective lines. *Mon. Wea. Rev.*, **133**, 2669–2691, https://doi.org/10.1175/MWR3002.1.

Kawashima, M., 2011: Numerical study of horizontal shear instability waves along narrow cold frontal rainbands. *J. Atmos. Sci.*, **68**, 878–903, https://doi.org/10.1175/2010JAS3599.1.

Knupp, K., 2006: Observational analysis of a gust front to bore to solitary wave transition within an evolving nocturnal boundary layer. *J. Atmos. Sci.*, **63**, 2016–2035, https://doi.org/10.1175/JAS3731.1.

Knupp, K. R., R. L. Clymer, and B. Geerts, 1996: Preliminary classification and observational characteristics of tornadic storms over northern Alabama. Preprints, *18th Conf. on Severe Local Storms*, San Francisco, CA, Amer. Meteor. Soc., 447–450.

Lee, B. D., and R. B. Wilhelmson, 1997a: The numerical simulation of non-supercell tornadogenesis. Part I: Initiation and evolution of pretornadic misocyclone circulations along a dry outflow boundary. *J. Atmos. Sci.*, **54**, 32–60, https://doi.org/10.1175/1520-0469(1997)054<0032:TNSONS>2.0.CO;2.

——, and ——, 1997b: The numerical simulation of non-supercell tornadogenesis. Part II: Evolution of a family of tornadoes along a weak outflow boundary. *J. Atmos. Sci.*, **54**, 2387–2415, https://doi.org/10.1175/1520-0469(1997)054<2387:TNSONT>2.0.CO;2.

Marchioro, C., and M. Pulvirenti, 1994: *Mathematical Theory of Incompressible Nonviscous Fluids.* Applied Mathematical Sciences Series, Vol. 96, Springer-Verlag, 284 pp.

Markowski, P., and Y. Richardson, 2010: *Mesoscale Meteorology in Midlatitudes*. Wiley-Blackwell, 430 pp.

Marquis, J. N., Y. Richardson, and J. Wurman, 2007: Kinematic observations of misocyclones along boundaries during IHOP. *Mon. Wea. Rev.*, **135**, 1749–1768, https://doi.org/10.1175/MWR3367.1.

Mohr, C. G., L. J. Miller, R. L. Vaughn, and H. W. Frank, 1986: The merger of mesocale datasets into a common Cartesian format for efficient and systematic analyses. *J. Atmos. Oceanic Technol.*, **3**, 143–161, https://doi.org/10.1175/1520-0426(1986)003<0143:TMOMDI>2.0.CO;2.

Mueller, C., and R. Carbone, 1987: Dynamics of a thunderstorm outflow. *J. Atmos. Sci.*, **44**, 1879–1898, https://doi.org/10.1175/1520-0469(1987)044<1879:DOATO>2.0.CO;2.

Oye, D. C., C. Mueller, and S. Smith, 1995: Software for radar translation, visualization, editing and interpolation. Preprints, *27th Conf. on Radar Meteorology*, Vail, CO, Amer. Meteor. Soc., 359–361.

Przybylinski, R. W., 1995: The bow echo: Observations, numerical simulations, and severe weather detection methods. *Wea. Forecasting*, **10**, 203–218, https://doi.org/10.1175/1520-0434(1995)010<0203:TBEONS>2.0.CO;2.

Rayleigh, L., 1879: On the stability, or instability, of certain fluid motions. *Proc. London Math. Soc.*, **s1-11**, 57–72, https://doi.org/10.1112/plms/s1-11.1.57.

Schenkman, A. D., M. Xue, and A. Shapiro, 2012: Tornadogenesis in a simulated mesovortex within a mesoscale convective system. *J. Atmos. Sci.*, **69**, 3372–3390, https://doi.org/10.1175/JAS-D-12-038.1.

Schneider, R., and A. Dean, 2008: A comprehensive 5-year severe storm environment climatology for the continental United States. *24th Conf. on Severe Local Storms*, Savannah, GA, Amer. Meteor. Soc., 16A.4, https://ams.confex.com/ams/24SLS/techprogram/paper_141748.htm.

——, ——, S. Weiss, and P. Bothwell, 2006: Analysis of estimated environments for the 2004 and 2005 severe convective storm reports. *23rd Conf. on Severe Local Storms*, St. Louis, MO, Amer. Meteor. Soc., 3.5, https://ams.confex.com/ams/23SLS/techprogram/paper_115246.htm.

Schultz, C. J., W. A. Petersen, and L. D. Carey, 2009: Preliminary development and evaluation of lightning jump algorithms for the real-time detection of severe weather.

J. Appl. Meteor. Climatol., **48**, 2543–2563, https://doi.org/10.1175/2009JAMC2237.1.

Sherburn, K. D., and M. D. Parker, 2014: Climatology and ingredients of significant severe convection in high-shear, low-CAPE environments. *Wea. Forecasting*, **29**, 854–877, https://doi.org/10.1175/WAF-D-13-00041.1.

Sun, L., 2007: General stability criterion of inviscid parallel flow. *Eur. J. Phys.*, **28**, 889–895, https://doi.org/10.1088/0143-0807/28/5/012.

Trapp, R., and M. L. Weisman, 2003: Low-level mesovortices within squall lines and bow echoes. Part II: Their genesis and implications. *Mon. Wea. Rev.*, **131**, 2804–2823, https://doi.org/10.1175/1520-0493(2003)131<2804:LMWSLA>2.0.CO;2.

——, S. Tessendorf, E. S. Godfrey, and H. Brooks, 2005: Tornadoes from squall lines and bow echoes. Part I: Climatological distribution. *Wea. Forecasting*, **20**, 23–34, https://doi.org/10.1175/WAF-835.1.

Wakimoto, R. M., and J. W. Wilson, 1989: Non-supercell tornadoes. *Mon. Wea. Rev.*, **117**, 1113–1140, https://doi.org/10.1175/1520-0493(1989)117<1113:NST>2.0.CO;2.

Weisman, M. L., and C. A. Davis, 1998: Mechanisms for the generation of mesoscale vortices within quasi-linear convective systems. *J. Atmos. Sci.*, **55**, 2603–2622, https://doi.org/10.1175/1520-0469(1998)055<2603:MFTGOM>2.0.CO;2.

——, and R. Trapp, 2003: Low-level mesovortices within squall lines and bow echoes. Part I: Overview and dependence on environmental shear. *Mon. Wea. Rev.*, **131**, 2779–2803, https://doi.org/10.1175/1520-0493(2003)131<2779:LMWSLA>2.0.CO;2.

Wheatley, D. M., and R. Trapp, 2008: The effect of mesoscale heterogeneity on the genesis and structure of mesovortices within quasi-linear convective systems. *Mon. Wea. Rev.*, **136**, 4220–4241, https://doi.org/10.1175/2008MWR2294.1.

Xu, X., M. Xue, and Y. Wang, 2015a: Mesovortices within the 8 May 2009 bow echo over the central United States: Analyses of the characteristics and evolution based on Doppler radar observations and a high-resolution model simulation. *Mon. Wea. Rev.*, **143**, 2266–2290, https://doi.org/10.1175/MWR-D-14-00234.1.

——, ——, and ——, 2015b: The genesis of mesovortices within a real-data simulation of a bow echo system. *J. Atmos. Sci.*, **72**, 1963–1986, https://doi.org/10.1175/JAS-D-14-0209.1.